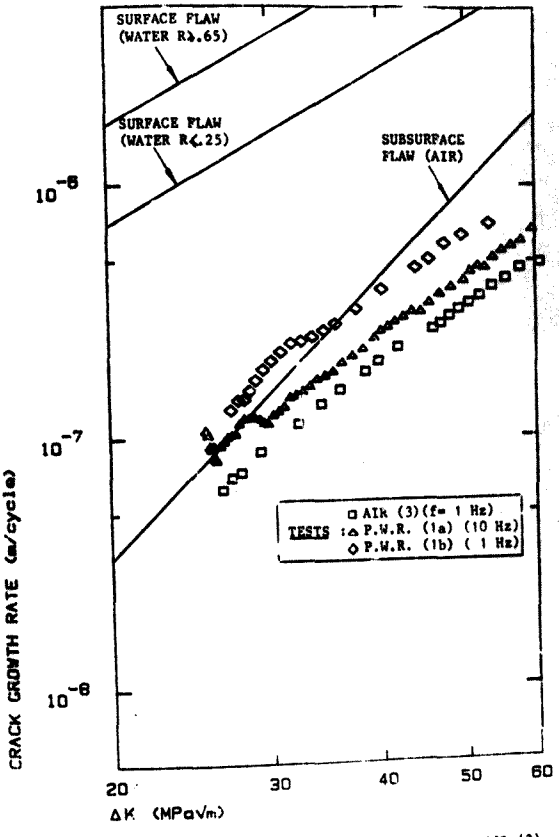

FIGURE 5.10: Combined da/dN versus ΔK curves for tests AIR (3), P.W.R. (1a) and P.W.R. (1b)

Test P.W.R. (1a)

PLATE 5.22: General microstructure showing ductile fracture surface 5 mm after crack initiation. (Mag. x 200)

Crack growth direction ↑

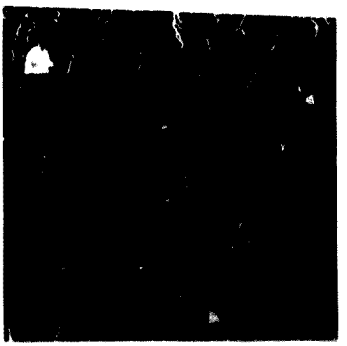

PLATE 5.23: General fracture surface. Ductile striated growth (enlarged region of above plate). (Mag. x 3000)

Crack growth direction ↑

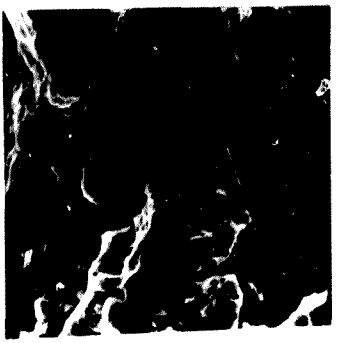

Test P.W.R. (1a)

PLATE 5.22: General microstructure showing ductile fracture surface 5 mm after crack initiation. (Mag. x 200)

Crack growth direction ↑

PLATE 5.23: General fracture surface. Ductile striated growth (enlarged region of above plate). (Mag. x 3000)

Crack growth direction ↑

PLATE 5.24: MnS stringer inclusion site initiating a local region of fan-shaped fast crack growth, although the enclosed region is still ductile (6 mm from crack initiation). (Mag. x 300)

Crack growth direction ↑

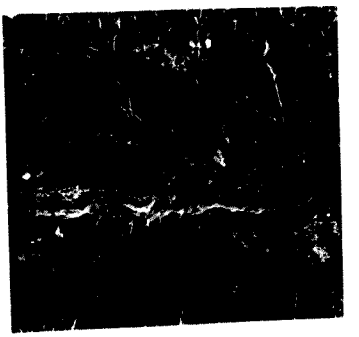

PLATE 5.25: Broken-up MnS with a region of fast crack growth before the crack has reached the inclusion. Large crack where the inclusion had been seated (4 mm after crack initiation). (Mag. x 100)

Crack growth direction ↑

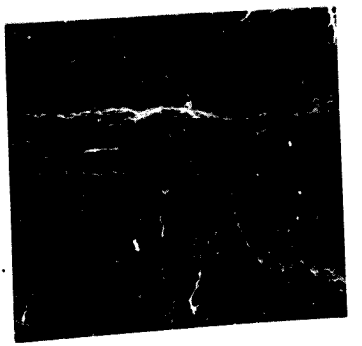

PLATE 5.26: Complete MnS present with relatively rapid crack growth after the inclusion. Note the terraced region where the crack has actually undergone ductile tearing down to the inclusion (1 mm after crack initiation). (Mag. x 450)

TEST P.W.R. 1(b)

PLATE 5.27: 'Broken-up' MnS with no adjacent 'fast' fracture regions. Occurrence found 5 mm from crack initiation. (Mag. x 120)

PLATE 5.28: General fracture surface showing a ductile striation mechanism of crack growth (8 mm from crack initiation). Mag. x 4500)

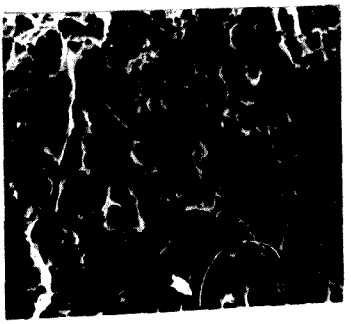

PLATE 5.29: MnS inclusion site with a 'comet' tail of smaller MnS inclusions (8 mm from crack initiation). Fast failure regions, about the inclusions, are linked via ductile tearing. (Mag. x 620)

PLATE 5.30: MnS inclusion region with fast crack growth before and after the inclusion (9 mm after crack initiation). (Mag. x 300)

5.2.3 P.W.R.(2a), (2b) and AIR (40R) orientation tests

These specimens were machined so that the fatigue crack growth took place in the normal (to through-thickness crack growth) direction. This corresponds to the 'worst' crack growth direction, since MnS stringers lie in the direction of crack growth.

Figure 5.11 shows test AIR(40R) and it can be seen that for $\Delta K < 34$ MPa $\sqrt{m}$ the crack growth rate is greater than that predicted by the ASME XI (1980) crack growth rate curve for subsurface flaw propagation in an air environment. Figure 5.12 combines the data for through-thickness crack growth and the orientation direction can be seen to increase the air crack growth rate by a factor of 2 for low ΔK crack growth.

Although the general crack growth mechanism is still ductile striated growth (Plate 5.31), plates 5.32 - 5.35 clearly show that elongated MnS inclusions have affected large regions of crack growth. Plate 5.32 shows the general fracture surface which has a marked 'terraced' appearance. This implies that the crack has actually been able to follow MnS inclusions even when they are not directly on the crack front fracture path, i.e. normal to the applied stress. This terraced appearance has led to regions of fast crack growth, thus explainirg the increase in crack growth rate above the specimen AIR(3) or (1) crack growth rates.

Figures 5.13 and 5.14 show the da/dN versus ΔK curves for the P.W.R. environment tests, 10 Hz and 1 Hz respectively. Both tests lie above the ASME air line data. The following two figures compare the P.W.R. environment tests with the orientation air test. Clearly both curves lie above the 'air' line curve for the same orientation tests. The following two figures (5.17 and 5.18) compare the orientation tests of the same frequency to the test for through-thickness crack growth. Both tests show higher growth rates compared to the through-thickness tests and the 10 Hz test in particular lies well above the P.W.R. (1a) test. The crack growth

rate is 2.3 times greater for the 10 Hz orientation test ($\Delta K = \pm 43$ MPa $\sqrt{m}$). The final figure (5.19) compares the 10 Hz and 1 Hz tests. It is obvious that both curves lie close to one another and for ΔK between 38 and 46 MPa $\sqrt{m}$, the 10 Hz test gave greater crack growth rates than the 1 Hz test. The reason for this can be seen from the S.E.M. fractographs of the two fracture surfaces.

Plates 5.37 - 5.45 clearly show that the fracture surface is 'riddled' with MnS inclusions which have assisted rapid crack growth. Large regions are linked together to provide a rapid crack growth path. Both the broken-up MnS and the 'whole' MnS's were seen to have the same effect on crack growth i.e. both creating fan shaped, fast crack growth regions.

Specimen P.W.R. (2b) does, however, not show these large MnS inclusion areas, but MnS alignment in the direction of crack growth is still evident (plates 5.49 - 5.52) which enhances crack growth above that observed for specimen P.W.R. (1b) where manganese sulphides are orientated normal to the crack growth direction.

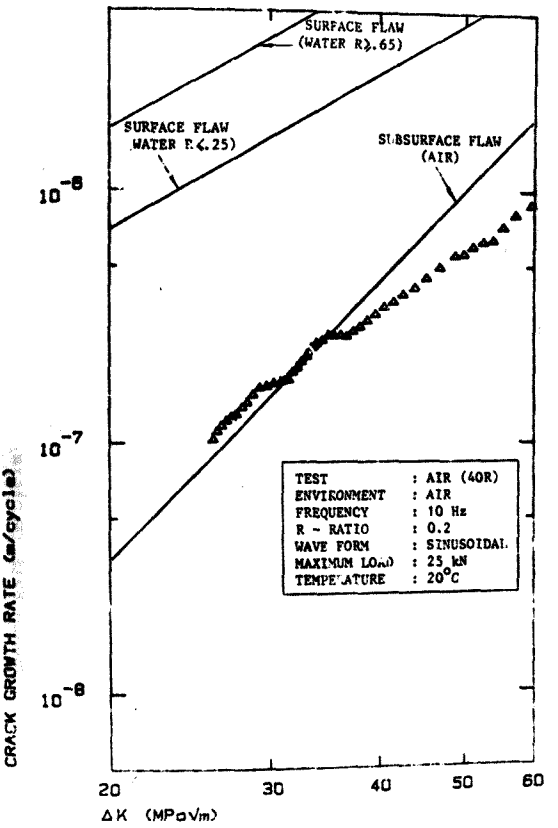

FIGURE 5.11: da/dN versus ΔK curve for test AIR (40R)

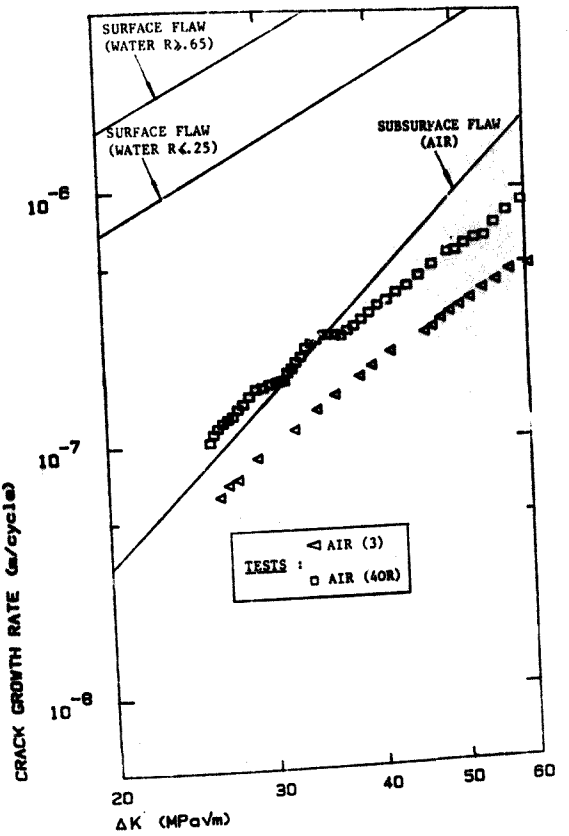

FIGURE 5.12: Combined da/dN versus ΔK curves for tests AIR (40R) and AIR (3)

PLATE 5.31: General fracture surface showing a ductile striation mechanism of crack growth (12 mm from crack initiation)
(Mag. x 1000)

PLATE 5.32: Terraced fracture surface with fanned regions originating from inclusions (10 mm from crack initiation).
(Mag. x 60)

PLATE 5.33: MnS stringers resulting in fanned regions of fast ductile crack growth (10 mm from crack initiation). (Mag. x 250)

PLATE 5.34: MnS stringers causing fast crack growth regions (12 mm from crack initiation). (Mag. x 300)

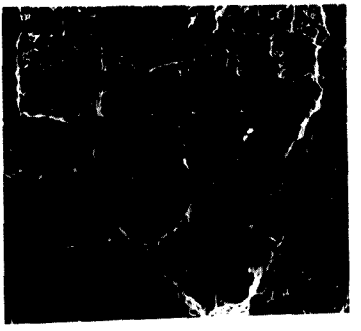

PLATE 5.35: Broken-up MnS stringer resulting in the same fan shaped, but ductile crack growth region (12 mm from crack initiation). (Mag. x 380)

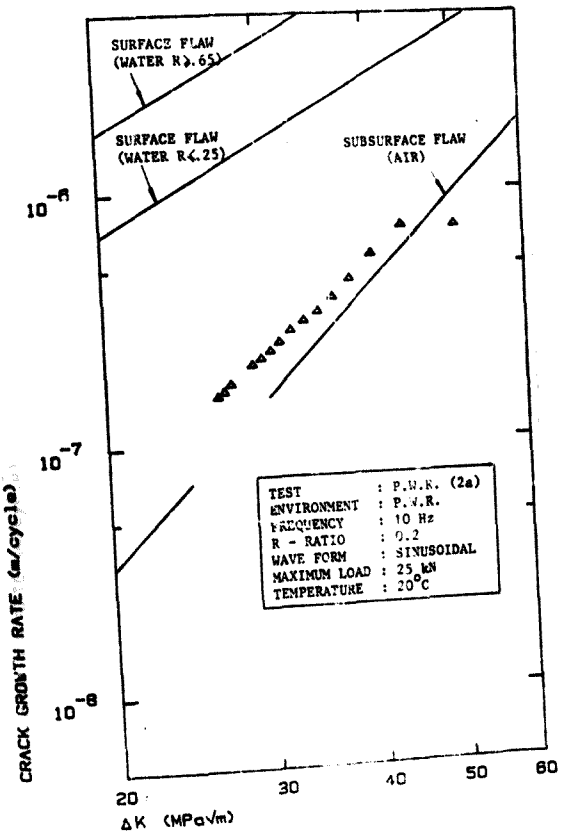

FIGURE 5.13: da/dN versus ΔK for test P.W.R. (2a)

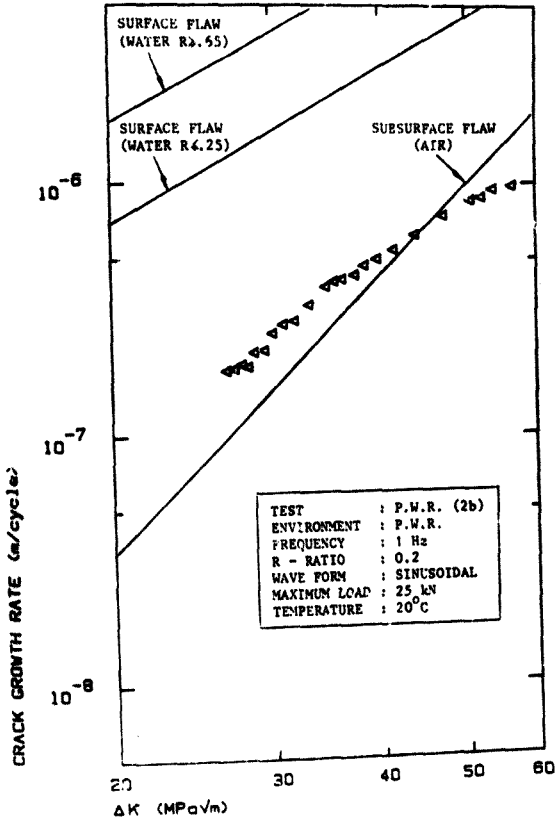

FIGURE 5.14: da/dN versus ΔK curve for test P.W.R. (2b)

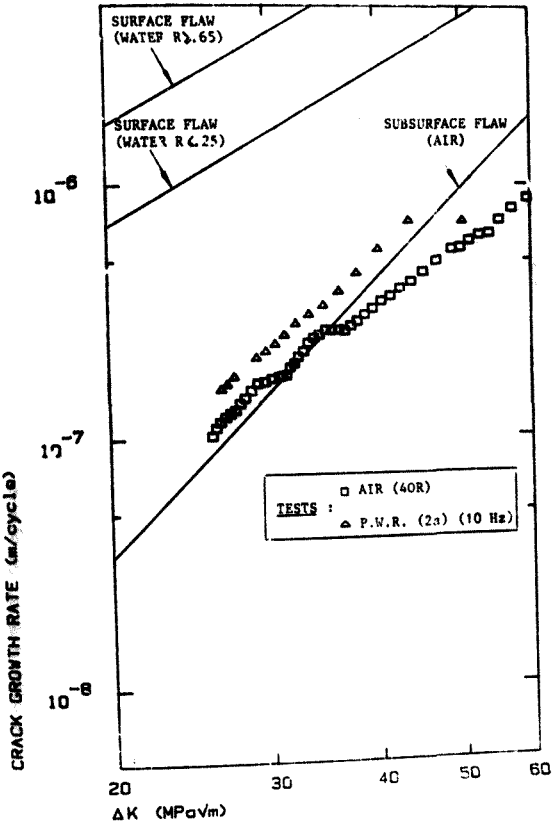

FIGURE 5.15: Combined da/dN versus ΔK curves for tests AIR (40R) and P.W.R. (2a)

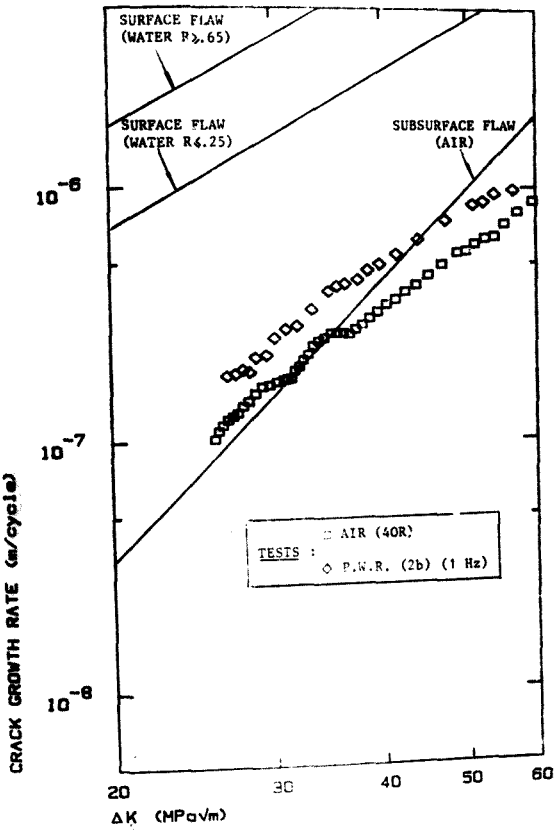

FIGURE 5.16: Combined da/dN versus ΔK curves for tests AIR (40R) and P.W.R. (2b)

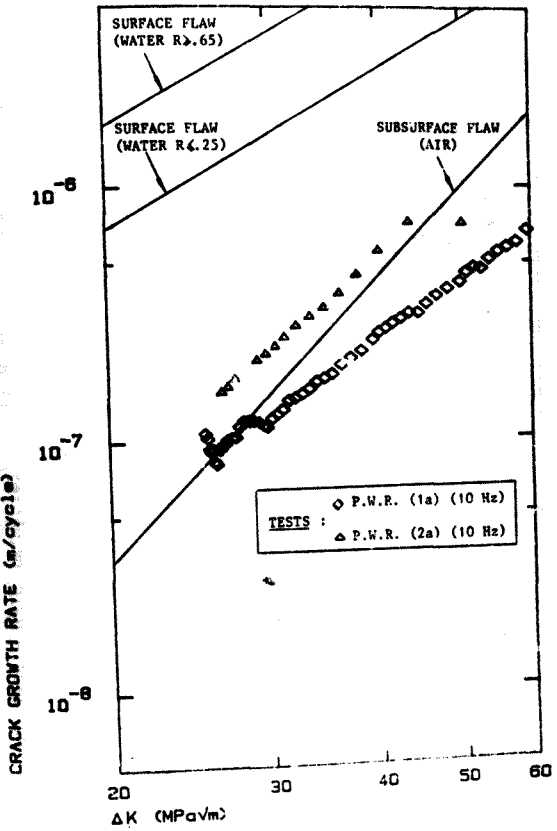

FIGURE 5.17: Combined da/dN versus ΔK curves for tests P.W.R. (1a) and P.W.R. (2a)

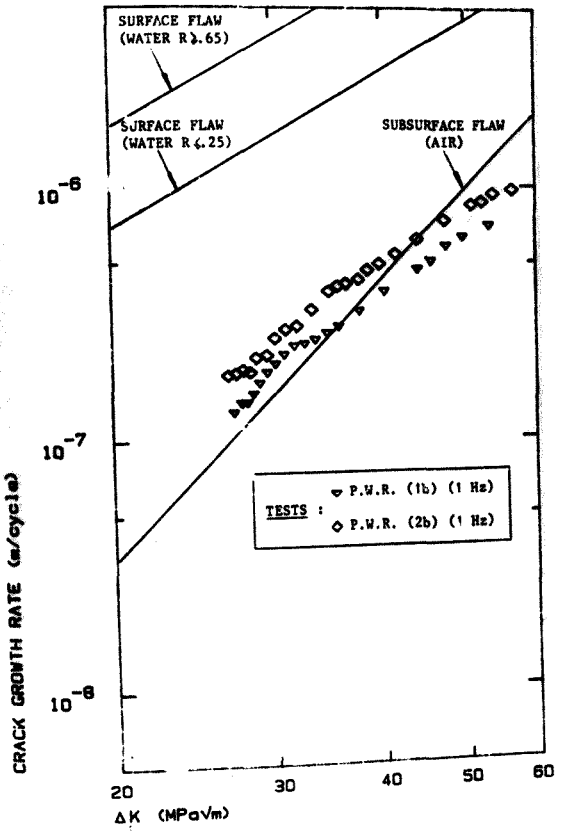

FIGURE 5.18: Combined da/dN versus ΔK curves for tests P.W.R. (1b) and P.W.R. (2b)

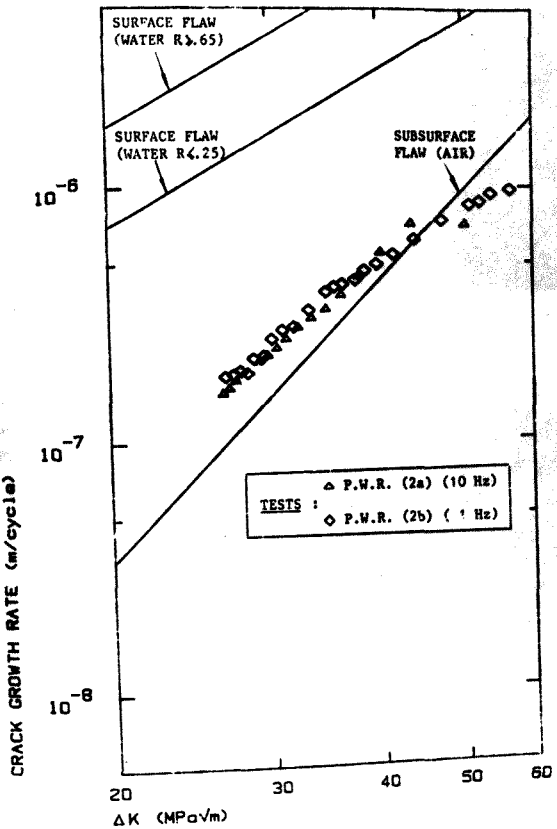

FIGURE 5.19: Combined da/dN versus ΔK curves for tests P.W.R. (2a) and P.W.R. (2b)

Test P.W.R. 2(a)

PLATE 5.36: General microstructure that is more brittle than through-thickness crack growth direction specimens (still ductile striated crack growth). (Mag. x 100)

PLATE 5.37: Fracture surface showing large regions
and
PLATE 5.38: of MnS st ngers. Fan shaped region, corresponding to rapid environmentally assisted crack growth. (Mag. x 20)

PLATE 5.38: (Mag. x 20)

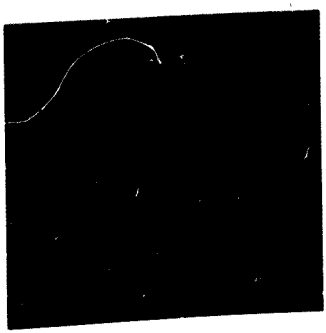

PLATE 5.39: MnS stringers with interlinking regions of fast brittle crack growth (typical chevron markings). (Mag. x 200)

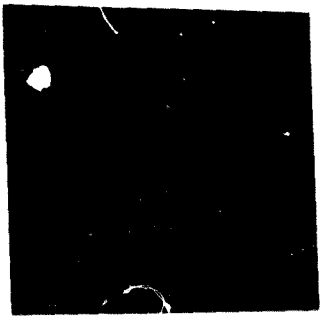

PLATE 5.40: Broken-up MnS leading to rapid crack growth. Environmentally assisted fan shaped growth originating from inclusions. (Mag. x 50)

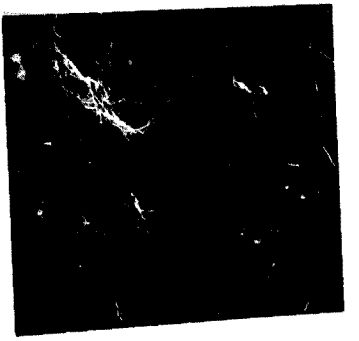

PLATE 5.41 - 5.45: Whole Mns inclusions seen at the base of fast fan shaped regions of crack growth.

PLATE 5.41: (Mag. x 100)

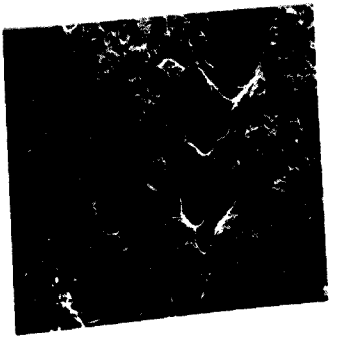

PLATE 5.42: (Mag. x 200)

PLATE 5.43: (Mag. x 200)

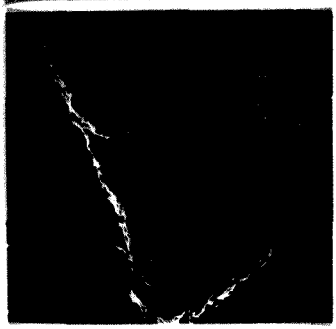

PLATE 5.44: (Mag. x 500)

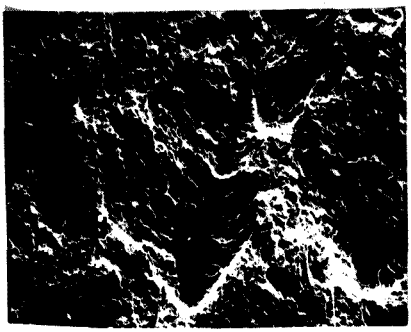

PLATE 5.45: (Mag. x 200)

PLATE 5.42: (Mag. x 200)

PLATE 5.43: (Mag. x 200)

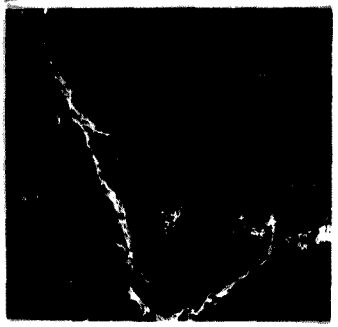

PLATE 5.44: (Mag. x 500)

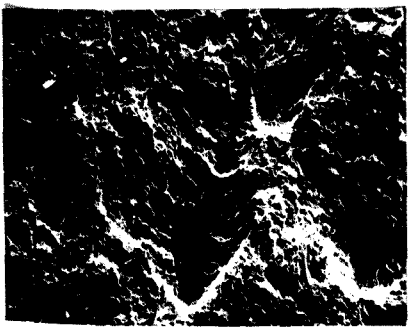

PLATE 5.45: (Mag. x 200)

Test P.W.R. (2b)

PLATE 5.46: Only a few regions of sulphide stringers and these are not [illegible]linked. (Mag. x 20)

PLATE 5.47: and 5.48: General microstructures that clearly show a more brittle fracture surface than for the through-thickness specimens. (Mag. x 200)

PLATE 5.48: General microstructure showing ductile striated crack growth. (Mag. x 600)

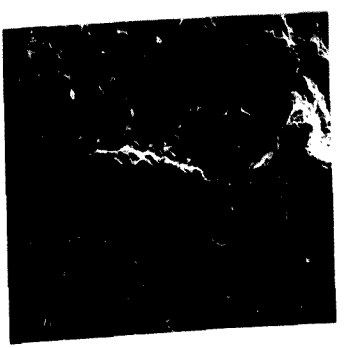

MnS inclusions resulting in fan shaped regions of fast crack growth

PLATE 5.49: (Mag. x 5000)

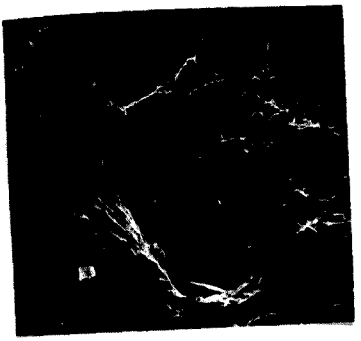

PLATE 5.50: (Mag. x 1000)

PLATE 5.51: (Mag x 1000)

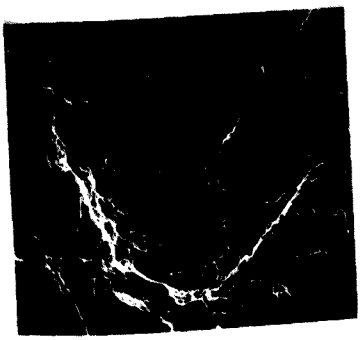

PLATE 5.52: (Mag. x 500)

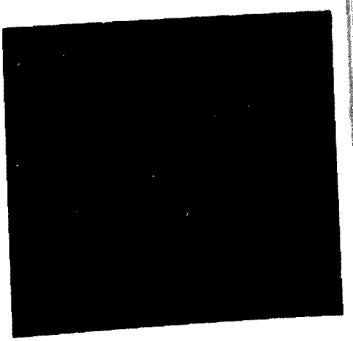

5.2.4 P.W.R. (3a) and (3b) tests

These tests were performed at 50 °C (as opposed to 20 °C) and Figs 5 and 5.21 show the da/dN versus ΔK curves for the 10 Hz and 1 Hz tests. Figure 5.22 combines the two curves with the air line data and it can clearly be seen that as the frequency of testing is reduced (10 Hz to 1 Hz), the crack growth rate is increased. An environmental effect is also observed at both frequencies.

Figures 5.23 and 5.24 compare the data to the 20 °C tests. The 10 Hz test shows a more marked effect of temperature, but still the temperature tests show that crack growth rates are accelerated by an increase in temperature from 20 to 50 °C. Clearly, for this steel the fractography cannot be ignored.

S.E.M. shows that the cracks grow in a ductile manner and MnS inclusions are present, lying normal to the crack growth direction. These inclusions do not always affect crack growth mechanisms but clearly their presence will cause a local increase in the crack growth rate.

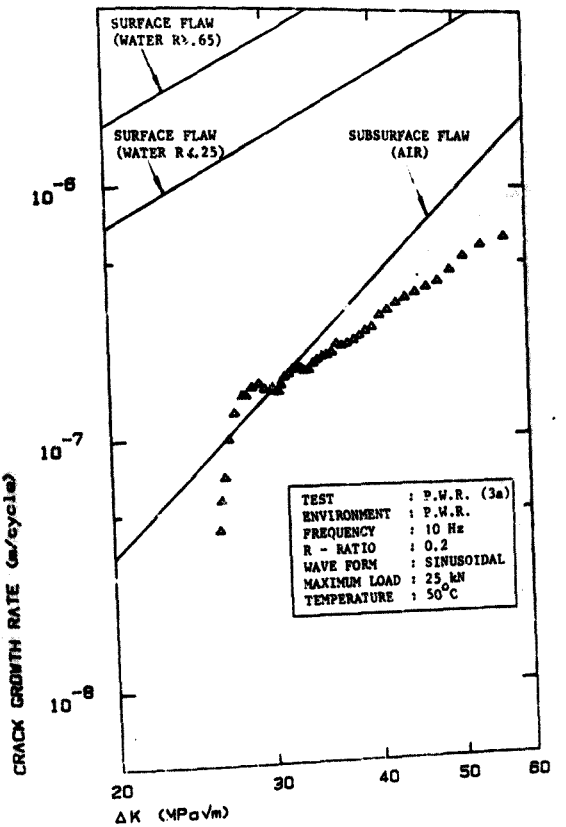

FIGURE 5.20: da/dN versus ΔK curve for test P.W.R. (3a)

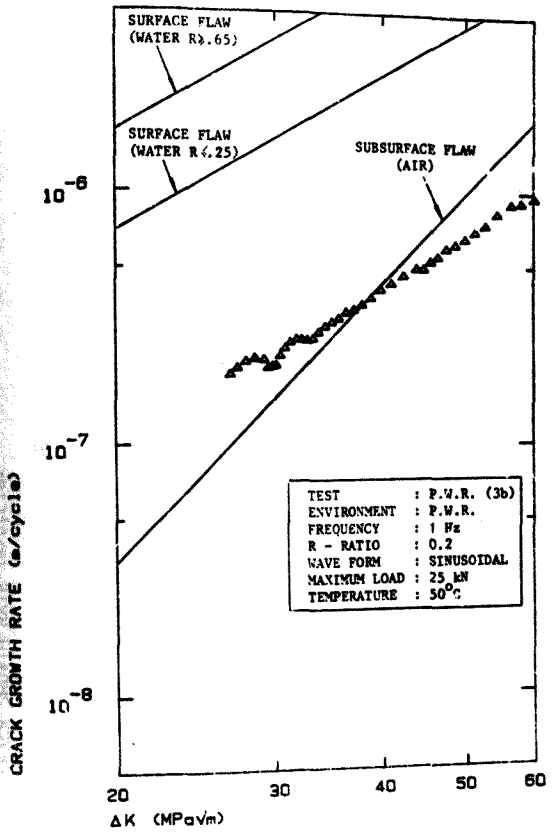

FIGURE 5.21: da/dN versus ΔK curve for test P.W.R. (3b)

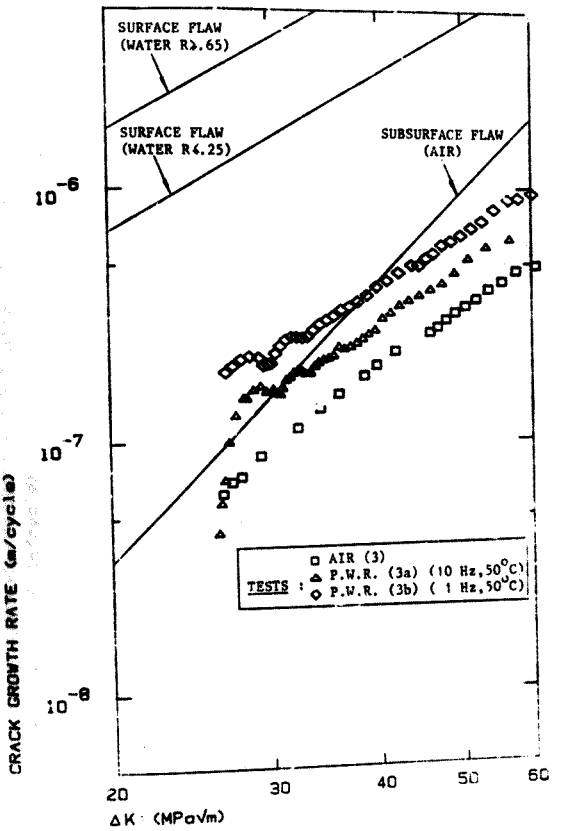

FIGURE 5.22: Combined da/dN versus ΔK curves for tests AIR (3), P.W.R. (3a) and P.W.R. (3b)

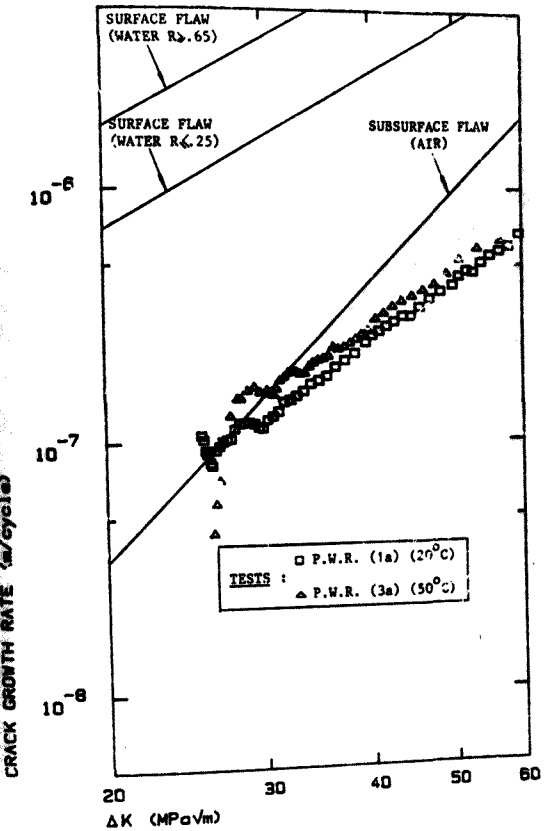

FIGURE 5.23: Combined da/dN versus ΔK curves for tests P.W.R. (1a) and P.W.R. (3a)

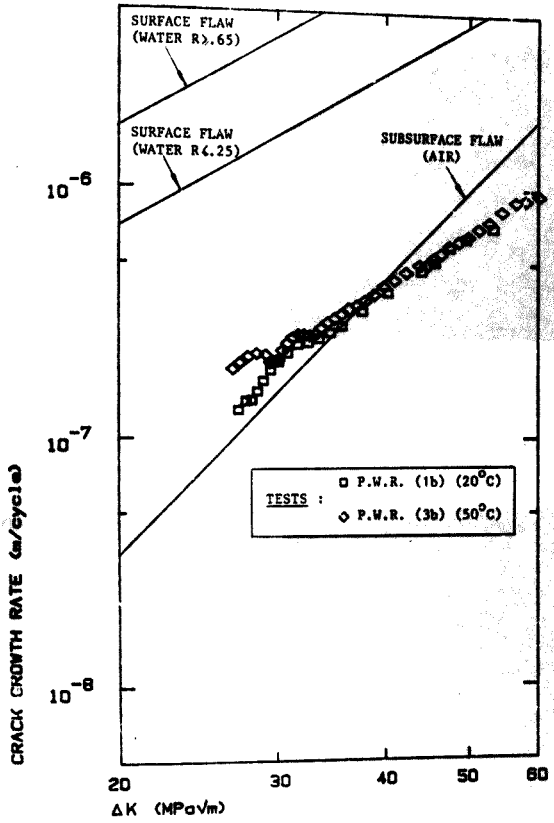

FIGURE 5.24: Combined da/dN versus ΔK curves for tests P.W.R. (1b) and P.W.R. (3b)

Test P.W.R. (3a)

PLATE 5.53: General fracture surface. More rapid crack growth mechanism (c.f. plate 5.22) but still predominantly ductile. (Mag. x 300)

PLATE 5.54: A region (±25 μm) of fast crack growth before the crack reaches the MnS ('broken-up') inclusion. Thereafter crack growth is typically via a ductile striation mechanism. (Mag. x 100)

PLATE 5.55: Showing MnS inclusions and inclusion sites. The presence of inclusions is not really affecting crack growth before or after the inclusion.
(Mag. x 2000)

PLATE 5.56: Regions of ductile crack growth visible about the Mns inclusion.
(Mag. x 160)

PLATE 5.57: Fast fan-shaped crack growth region originating from an inclusion cluster.
(Mag. x 450)

PLATE 5.58: Crack growth via a brittle cleavage mechanism after the inclusion. Still, however, regions of ductile cleavage failure are evident between the 'steps' of brittle failure. (Mag. x 600)

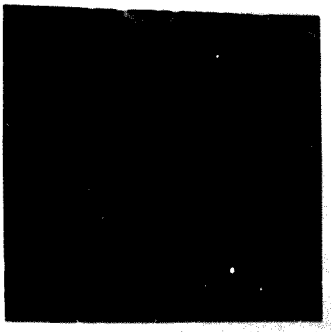

PLATE 5.59: 'Broken-up' MnS inclusion affecting crack growth locally. Note the small brittle facetted region and related fan-shaped growth. (Mag. x 200)

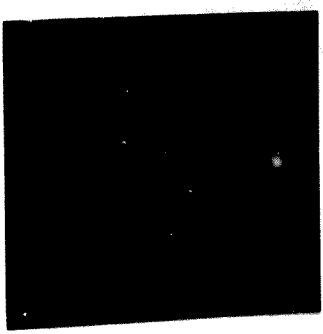

Test P.W.R (3b)

PLATE 5.60: General fracture surface identical to that of the P.W.R. (3a) test piece. (Mag. x 420)

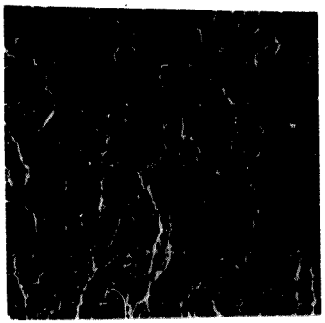

PLATES 5.61 and 5.62: MnS inclusion sites forming a terraced crack growth region. The crack front has had to drop to the level of the MnS the presence of which has been 'sensed' by the crack front. The crack then extends into a local region of environmentally assisted fan-shaped growth.

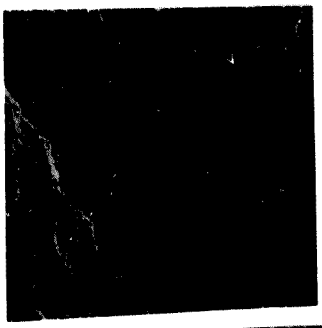

PLATE 5.61: (Mag. x 300)

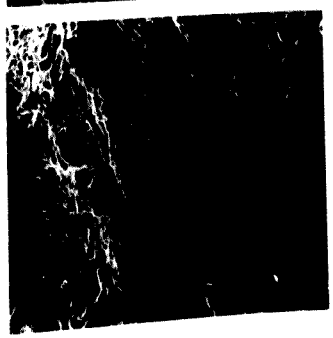

PLATE 5.62: (Mag. x 300)

PLATE 5.63 - 5.65: MnS inclusions showing that the MnS inclusions need to lie close to one another to really cause a faster crack growth morphology. This morphology need not only occur between the sulphides. (Mag. x 300)

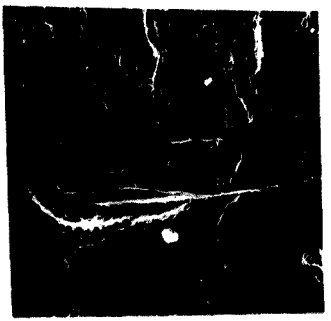

PLATE 5.64: Fan-shaped regions of crack growth originating from the inclusion clusters. (Mag. x 300)

PLATE 5.65: Faster crack growth region extending slightly past the final MnS inclusion. (Mag. x 300)

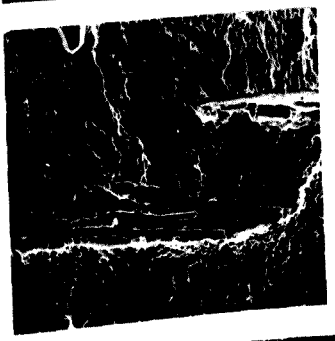

5.2.5 P.W.R. (4a), (4b) and AIR(2) tests

These experiments were all carried out at an R-ratio of 0.7 (as opposed to R = 0.2 for all other tests). Figure 5.25 shows the air test and it is immediately obvious that the data lies above the ASME XI (1980) 'dry' curve. For low ΔK values (± 9 MPa $\sqrt{m}$) the air data was even above the P.W.R. ($R < 0.25$) curve (ASME code). Figure 5.26 combines the da/dN versus ΔK curves for the 0.2 R-ratio tests and the 0.7 R-ratio test. Clearly the ASME curves could require revision for fatigue testing in air.

S.E.M. analysis shows that this rapid crack growth rate at low ΔK can be explained by the presence of bands of inclusions found near the crack front (4 mm from the crack initiation point) i.e. 0.5 mm from the prefatigue crack front.

Figures 5.27 and 5.28 show the curves for the 1 Hz and 10 Hz P.W.R. environment tests. As expected, both curves lie below the ASME $R \geq 0.65$ 'water' curve. Figure 5.29 shows both the curves and it can be seen that the 10 Hz test, which initially shows a plateau behaviour, gives faster crack growth rates for low ΔK ($\Delta K < \pm 12$ MPa $\sqrt{m}$) and high ΔK ($\Delta K > \pm 20$ MPa $\sqrt{m}$) than for the 1 Hz test. The 1Hz test shows an initial fast crack growth rate but then, forms a plateau. Both curves show a change in crack growth rate versus ΔK behaviour at $\Delta K = 15$ MPa $\sqrt{m}$. The two curves have been compared to the 0.7 R-ratio air test in Figs. 5.30 and 5.31. Figures 5.30 and 5.31 show that the air test exhibits a faster crack growth rate than either P.W.R. tests, for high ΔK values. Figures 5.32 and 5.33 compare the 0.7 R-ratio tests to the 0.2 R-ratio tests of similar frequencies.

These occurrences of inverse behaviour (at $\Delta K = \pm 15$ MPa $\sqrt{m}$) could be explained using the fractographic evidence. (See plates 5.71 - 5.83.)

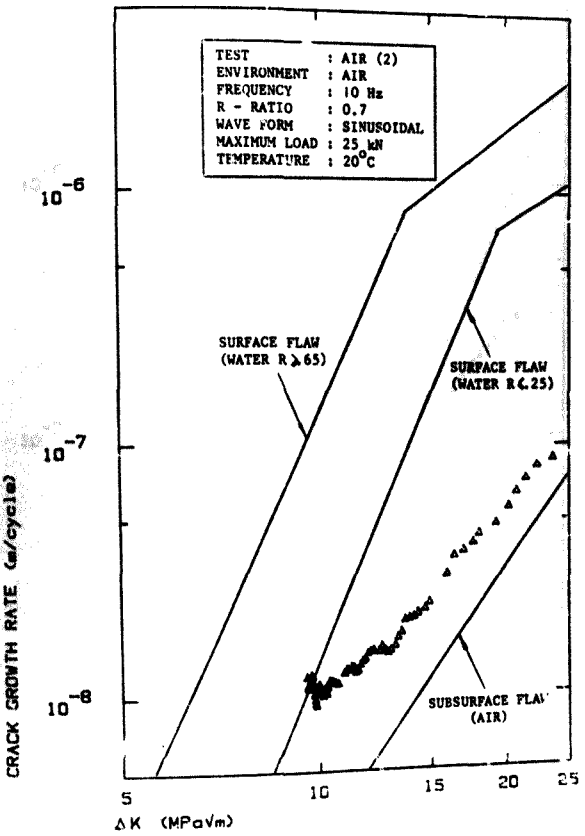

FIGURE 5.25: da/dN versus ΔK curve for test AIR (2)

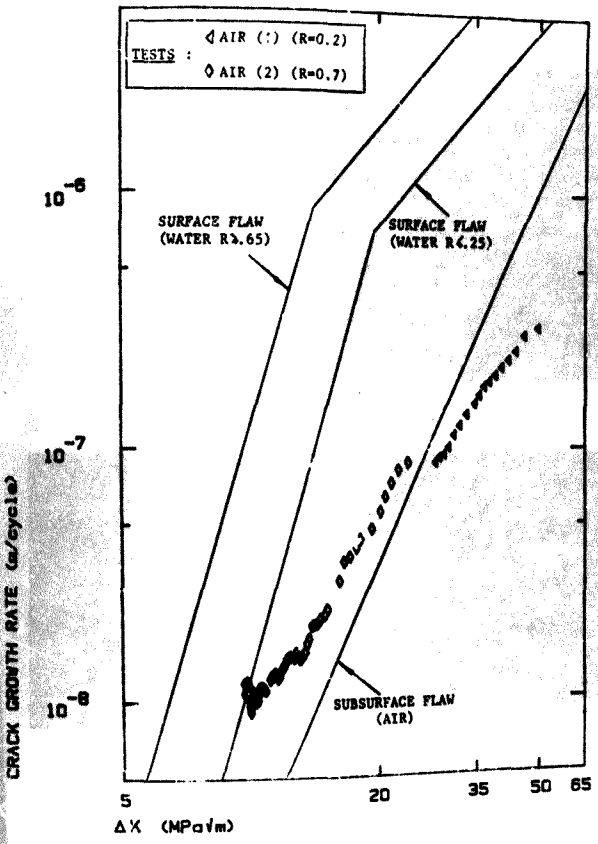

FIGURE 5.26: Combined da/dN versus ΔK curves for tests AIR (1) and AIR (2)

Test AIR (2)

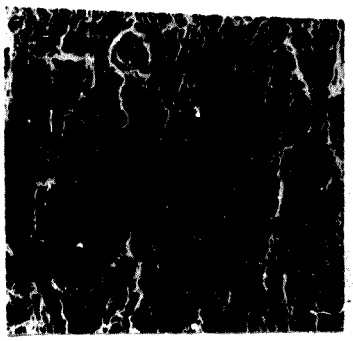

PLATE 5.66: General fracture surface showing fractographic features similar to those found in P.W.R. tests.
(Mag. x 400)

PLATE 5.67: Large regions of MnS stringers which explain why the crack growth rates are so high for the AIR (2) test at low ΔK levels.
(Mag. x 60)

PLATES 5.68 - 5.70: MnS stringer regions which would give rise to rapid crack growth.

PLATE 5.68: (Mag. x 300)

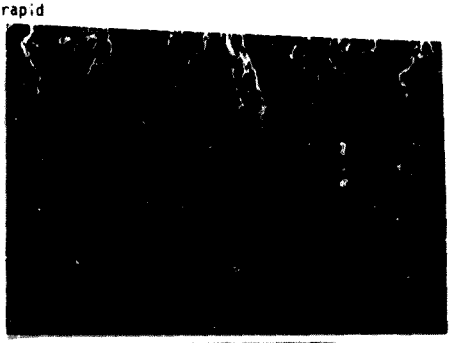

PLATE 5.69: (Mag. x 400)

PLATE 5.70: (Mag. x 600)

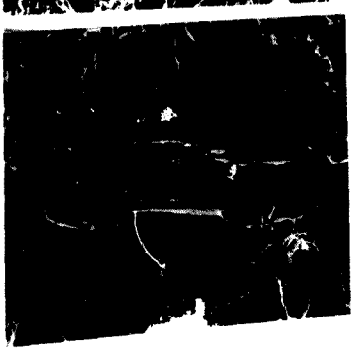

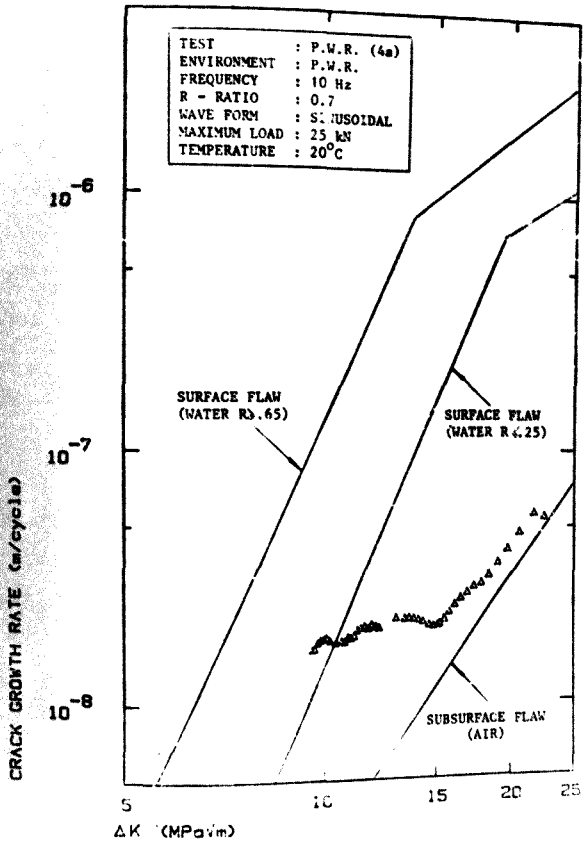

FIGURE 5.27: da/dN versus ΔK curve for test P.W.R. (4a)

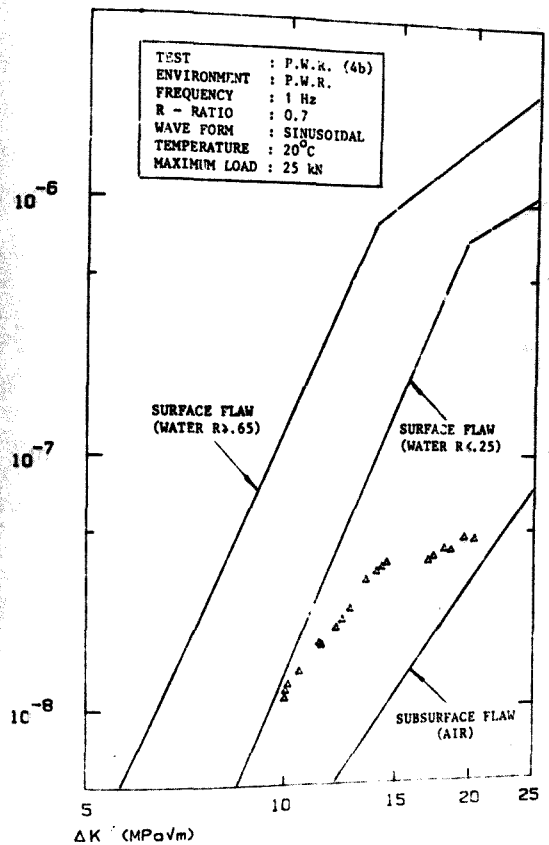

FIGURE 5.28: da/dN versus ΔK curve for test P.W.R. (4b)

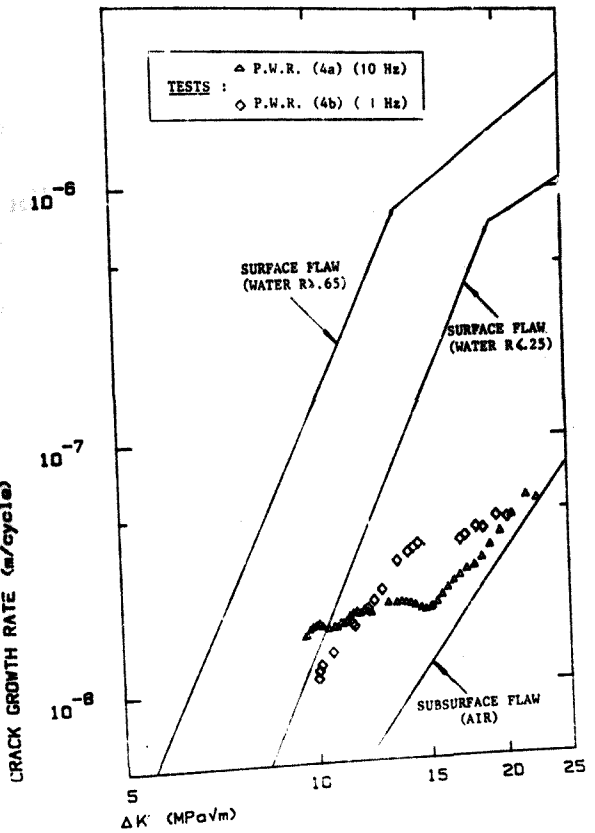

FIGURE 5.29: Combined da/dN versus ΔK curves for tests P.W.R. (4a) and P.W.R. (4b)

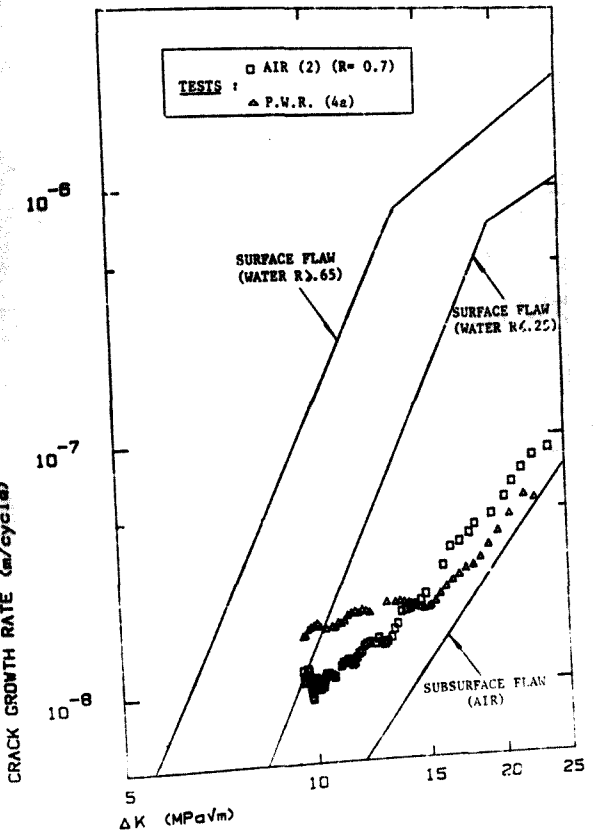

FIGURE 5.30: Combined da/dN versus ΔK curves for tests AIR (2) and P.W.R. (4a)

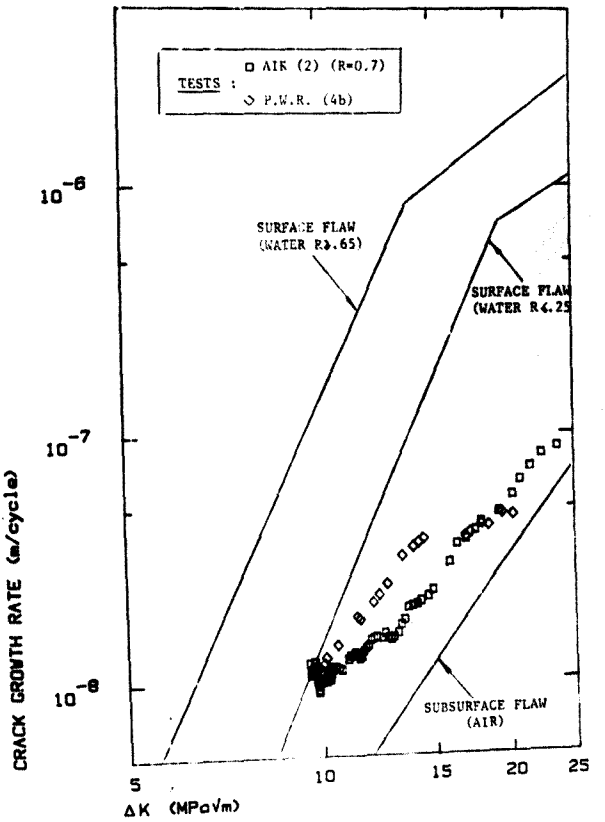

FIGURE 5.31: Combined da/dN versus ΔK curves for tests AIR (2) and P.W.R. (4b)

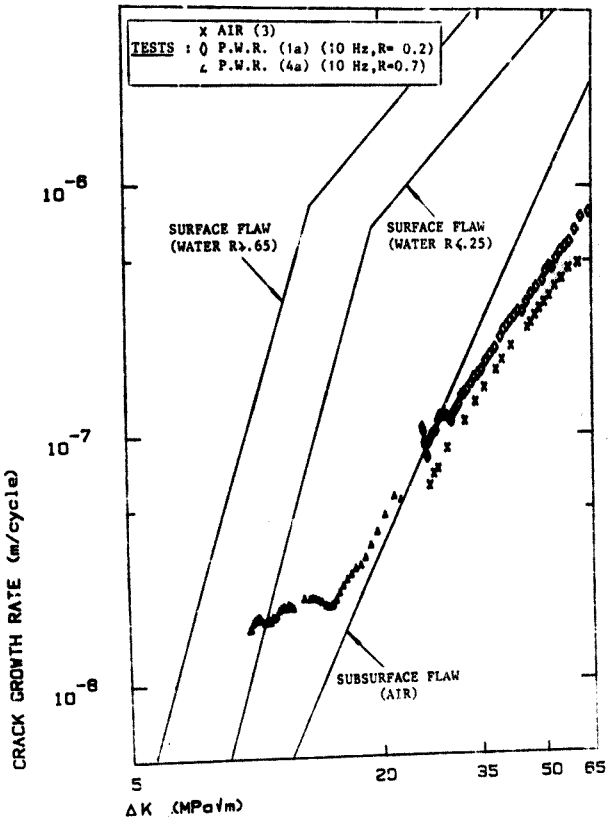

FIGURE 5.32: Combined da/dN versus ΔK curves for tests AIR (3) P.W.R. (1a) and P.W.R. (4a)

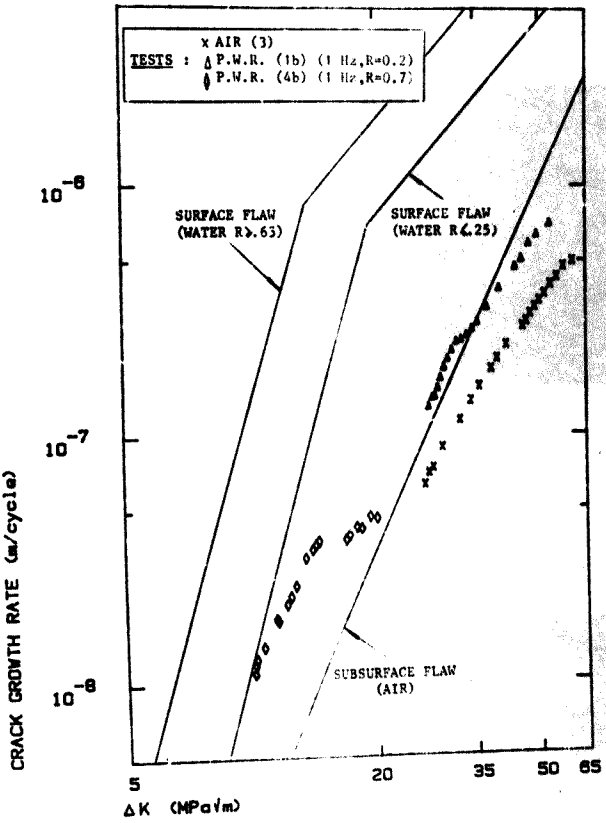

FIGURE 5.33: Combined da/dN versus ΔK curves for tests AIR (3), P.W.R. (1b) and P.W.R. (4b)

Test F.W.R. (4a)

PLATES 5.71: Showing general fracture surface about initiation of crack growth. Clearly, crack advancement is by a ductile striation mechanism. (Mag. x 1000)

and 5.72:

Plate 5.72: Close-up of the above fracture surface. (Mag. x 3000)

PLATES 5.73 - 5.75: Crack growth morphology at (ΔK = ±15 MPa $\sqrt{m}$) corresponds to facets of fast failure (cleavage) amongst ductile regions. The final plate shows a typically intergranular type of attack.

Plate 5.73: (Mag. x 500)

Plate 5.74: (Mag. x 600)

Plate 5.75: (Mag. x 600)

PLATES 5.76 - 5.78: MnS inclusions found towards the end of crack growth explain why crack growth rates increased dramatically for the 10 Hz test.

Plate 5.76: (Mag. x 500)

PLATE 5.77: Note fanned region originating from an inclusion site. (Mag. x 1000)

Plate 5.78: (Mag. x 300)

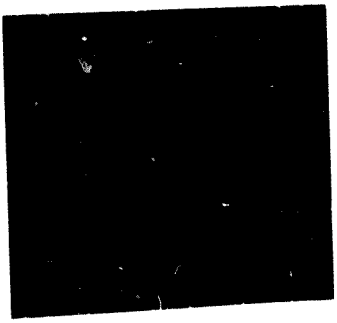

TEST P.W.R. (4b)

PLATE 5.79: General microstructure 2 mm from the pre-fatigued crack growth region. More rapid ductile growth could explain the initial fast crack growth rate variation with ΔK. (Mag. x 1000)

PLATES [illegible] re regions [illegible] and 5.81 [illegible] MPa√m [illegible]. These [illegible] es correspond [illegible] those found [illegible] ly [illegible], i.e. brittle. [illegible] granular regions of failure flanked by ductile crack growth.

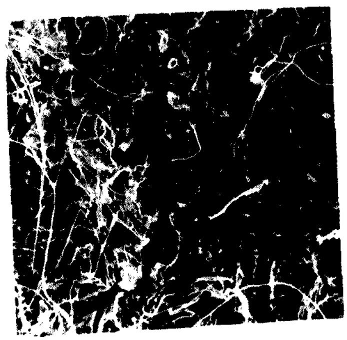

Plate 5.80: (Mag. x 600)

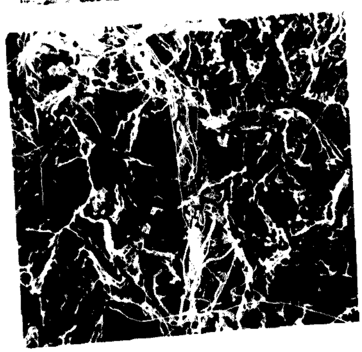

Plate 5.81: (Mag. x 600)

PLATES 5.82 and 5.83: MnS inclusions appear to have no influence on the crack growth mechanism in the adjacent matrix. Photographs were taken 1 mm from the final fracture surface.

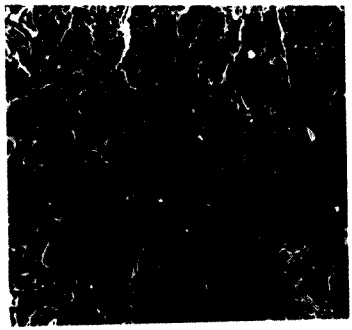

Plate 5.82: (Mag. x 600)

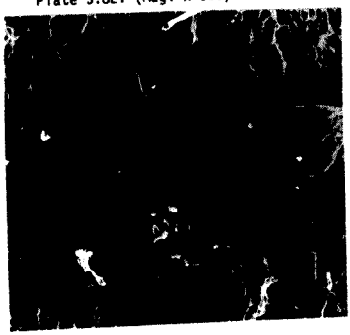

Plate 5.83: Small regions of fan-shaped growth after the MnS inclusions.
Mag. x 400

5.3 Potentiodynamic Curves and C.T. Specimen Potential Monitoring

SA508 material shows no passive region on potentiodynamically scanning from -200 mV (relative to E_{corr}) to 1100 mV (S.C.E.) in a P.W.R. environment. A current density of 127 $\mu A/cm^2$ corresponds to a voltage of 0.000 V (S.C.E.). (See Fig. 5.34.)

The freely corroding potential (E_{corr}) for SA508 at 20 °C is -674 mV (S.C.E.). E_{corr} = -649 mV (S.C.E.) for SA508 at 50 °C. The clevis (for C.T. specimens) is manufactured from AISI type 316 stainless steel, and E_{corr} for 316 stainless steel in a P.W.R. environment was found to be -376 mV (S.C.E.).

Linear polarization (at 20 °C) showed that the general corrosion rate corresponding to an E_{corr} of -674 mV (S.C.E.), was 6.37 mpy (0.16 mm per year).

Sample potential recording using a calomel electrode and a Luggin probe was carried out for five corrosion fatigue tests. These included the orientation and temperature tests as well as the 1 Hz, R = 0.2, sinewave, room temperature test. The results are plotted for two of the tests, one at 20 °C and the other at 50 °C (Fig. 5.35). It was found for all the potential monitoring tests that the sample potential only varied with temperature. The results plotted on Fig. 5.35 have not been compensated for a temperature correction i.e. the results correspond to the direct S.C.E. reading at the particular temperature of interest (20 °C or 50 °C).

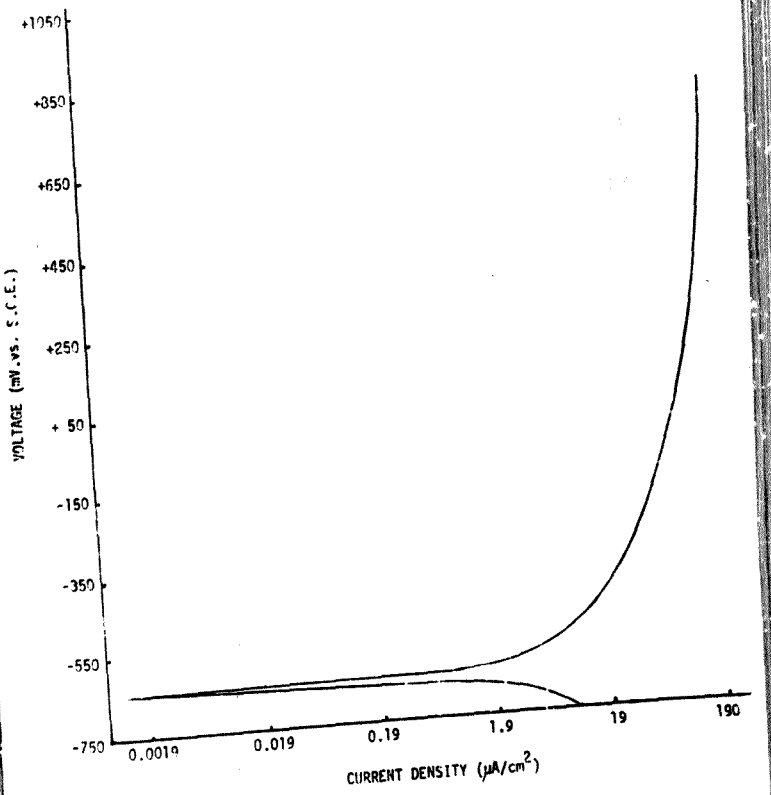

FIGURE 5.34: Potentiodynamic polarization curve for SA-508 pressure vessel steel in a P.W.R. environment (20 °C)

FIGURE 5.35 : SPECIMEN POTENTIAL VARIATION WITH CRACK LENGTH

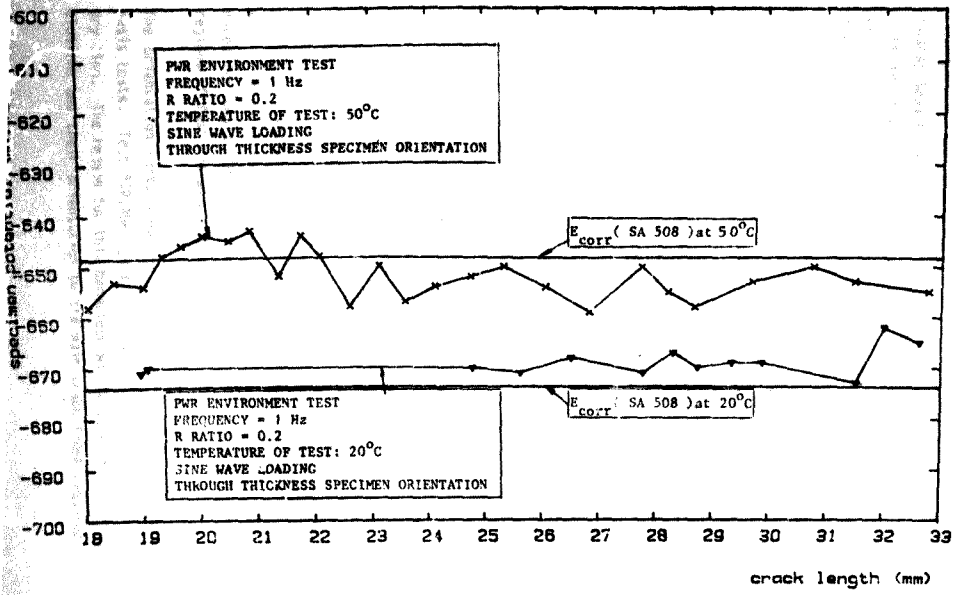

5.4 Summary

Charpy impact testing showed that a definite orientation effect exists for the forged nozzle region (through-thickness crack growth: Charpy impact energy = 268 J versus 154 J for orientation samples). Tensile tests showed no effect of orientation (σ_Y = 492 MPa, $\sigma_{U.T.S.}$ = 626 MPa, El = 22.87%; R.A. = 69.15%) and hardness testing also showed little effect of orientation (Hyp_N = 227).

The chemical composition of the steel was typical of a wrought 0.16% C (1.38 Mn, 0.77 Ni, 0.52 Mo) low alloy pressure vessel steel. The microstructure corresponding to segregated (dark) regions and light regions of upper bainite. These dark regions contained the MnS stringers and lay in the working direction. Macroscopy and sulphur printing showed that large 'plates' of MnS stringers are present (the MnS lying in orientation B and the 'stacking' direction being in orientation C).

The corrosion fatigue tests were carried out in an environment that simulated P.W.R. conditions within a nuclear reactor (K<25 $\mu S.cm^{-1}$; pH = 6.5 ± 0.2; O_2 < 10 ppb; F^- < 40 ppb; Cl^- < 120 ppb; B = ±900 ppm; Li = ±1.6 ppm; H_2 = 5.5 - 21.7 std.cc/kg H_2O; SO_4^{2-} < 30 ppb).

The air tests (AIR(1) and (3)) both produced da/dN versus ΔK curves lying below the ASME dry line and the crack propagation mode was found to be ductile striated growth. The 'basis' tests P.W.R. (1a) and (1b) showed environmentally enhanced crack growth. This was more pronounced for the lower frequency test, but enhancement was noted for the 10 Hz test. MnS inclusions have resulted in local regions of fast fan-shaped crack growth.

The orientation tests showed a faster crack growth rate than the basis tests. Test AIR(40R) gave crack growth rates above the ASME dry line. The reason for this behaviour was because of the MnS inclusions and their orientation to the main crack front resulted in

fanned, terraced regions of fast crack growth. The 10 Hz and 1 Hz P.W.R. tests showed fast crack growth (fan-shaped) fractographic features and both tests gave higher crack growth rates than the air test. MnS inclusions aided fast crack growth, this being particularly noticeable in the 10 Hz test.

Both temperature tests (50 °C) gave crack growth rates marginally above those observed for the 20 °C tests. Thus, an environmental enhancement effect was observed and this effect was greater for the 1 Hz test. Regions of fast crack growth, about MnS inclusions, were visible for both the tests.

The 0.7 R-ratio air test produced crack growth rates greater than the ASME Air line data. This was as a result of bands of MnS inclusions (found on the surface) aiding crack growth. The inclusions have resulted in ductile striated crack growth morphology. The 0.7 R-ratio environment tests (10 Hz and 1 Hz) showed an inverse behaviour at $\Delta K = \pm 15$ MPa $\sqrt{m}$. Both fracture surfaces showed regions of intergranular failure in this ΔK régime. Fractographic features can explain why the 10 Hz test initially showed a plateau behaviour and then an increase in crack growth rate with ΔK. The 1 Hz test only showed a plateau behaviour at a later stage ($\Delta K > 15$ MPa $\sqrt{m}$).

Potential monitoring studies indicated that the potential recorded during the corrosion fatigue tests corresponded to the freely corroding potentials for SA508 C13 steel, at the temperature of testing.

6.0 DISCUSSION

6.1 Metallurgical Data for Low Alloy Mn-Ni-Mo Pressure Vessel Steels

SA508 C13 is a Mn-Ni-Mo low alloy steel listed in Section II of the ASME Code as a nuclear pressure vessel steel. The nuclear reactors, installed at Koeberg (Cape Town), were manufactured in France by Framatome and details of the specified chemical composition and mechanical properties of the SA508 C13 forged steel are given in Table 6.1. Included in Table 6.1 are the average chemical composition and tensile properties for this series of tests and for SA533 GrB C11 steel. The latter steel is the 'rolled' equivalent of the forged SA508 C13 steel. (Each material is used in the manufacture of different sections of the nuclear reactor.)

Clearly, the SA508 C13 nozzle section, used for these experiments, conforms to specification.

A number of limitations has been made with regard to the ASTM standards. These limitations are based on the following considerations:

a) Limitation of the maximum carbon content to 0.22%. Improvement in weldability (and toughness).

b) Restrictions on the sulphur and phosphorous contents. Improvement in toughness (transition and upper shelf).

c) Limits on the contents of copper, cobalt and other residual elements. The copper and phosphorous content is limited to minimize the effect of irradiation embrittlement on the belt line materials. The cobalt content is limited to minimize radioactivity of the vessel walls after a period of operation. As, Sb and Sn are found at low residual levels owing to the precautions taken to reduce other residual elements.

TABLE 6.1: Chemical and Tensile Requirements for Nuclear Reactor Pressure Vessel Steels

A. CHEMICAL REQUIREMENTS (product analysis)

Element (a)	SA533 Gr B Cl1	SA508 Cl3	This Test Series (SA508 Cl3)
C	0.22 max	0.22 max	0.16
Mn	1.10/1.55	1.12/1.58	1.38
P	0.025 max	0.025 max (b)	0.013
S	0.025 max (c)	0.025 max (c)	0.008
Si	0.13/0.32	0.11/0.39	0.25
Ni	0.37/0.73	0.37/0.83	0.77
Cr	0.25 max	0.30 max	0.26
Mo	0.41/0.64	0.40/0.65	0.52
Cu	0.25 max (c)	0.25 max (b,c)	0.06
V	0.04 max (d)	0.04 max (d)	0.013

(a) min/max

(b) For core shells
P < 0.015% Cu < 0.10%
For Nozzle shells and Nozzles
P < 0.017 Cu < 0.12

(c) For reactor vessel:
S < 0.20% Cu < 0.20%

(d) For SA533 B Cl1 and SA508 Cl3 cladded components V <0.01%

B. TENSILE REQUIREMENTS FOR SA508 Cl3 and SA533 gr B Cl1

20 °C				343 °C	360 °C	
R 0.002 (MPa)	Rm (MPa)	A% (5d)	Z%	R 0.002 (MPa)	R 0.002 (MPa)	
345	552/666	18	38	286	282	
492.6	625.8	22.8	69.2			← SA508 Cl3 for this test series

d) A Limit on the vanadium content in ord to improve the resistance to underclad reheat cracking.

e) Austenitic grain growth is avoided by aluminium killing of the melt.

After forging and quenching, the nozzle section undergoes typical preliminary heat treatment [55] which consists of:

- furnace cooling to 350 °C immediately after forging
- austenitizing at 900 - 950 °C
- air cooling to 350 °C
- tempering at approximately 650 °C followed by furnace or air cooling.

A typical quality heat treatment procedure for heavy forgings is shown in Fig. 6.1. This is carried out on a part that has been rough machined.

6.1.1 Change in properties with thickness and anisotropism due to thermal and mechanical treatments

Forging or rolling operations induce a preferred orientation of the inclusions, such as sulphides, in the working direction. The effect is related to the relative inclusion matrix plasticity and differs according to whether the inclusions are harder than the matrix and do not deform (oxides), or whether they are softer than the matrix and therefore are easily elongated (e.g. MnS). Hot working also produces a preferred orientation of the zones of minor segregation which occurs during solidification of the ingot.

Since the physical and mechanical properties of the structure are not isotropic for all the compounds involved, the result is for anisotropism of the mechanical properties on the macroscopic scale.

FIGURE 6.1: QUALITY HEAT TREATMENT (55)

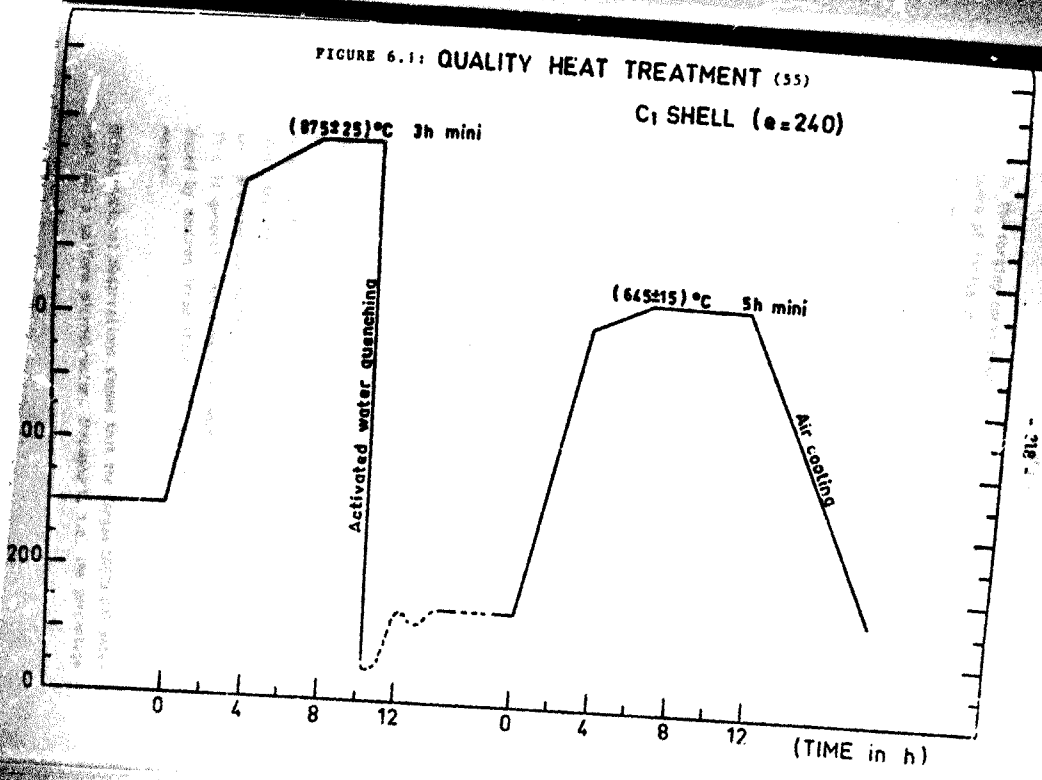

In the forging considered, the anisotropism resulting from the presence of inclusions is a major cause of variations in impact properties.

The presence of a pronounced directional effect can be recognized by the fact that the Charpy impact strength values obtained from specimens resulting in crack growth in the transverse direction are higher (268 J), than those obtained from specimens resulting in crack growth in the longitudinal direction (154 J).

This reduction in CVN impact strength is more important at the upper shelf of the Charpy transition curve. It is, of course, a function of the forging ratio related to the longitudinal and transverse working directions, and of the sulphur content. (The ductile-to-brittle transition temperature for SA508 Cl3 material is about 0 °C.)

Through-thickness properties result from the change in metallurgical microstructure between the surface and the core of the part, which is induced by the variation in the quenching rates. All the mechanical properties vary slightly, but the greatest variation is in the impact strength values.

The mechanical properties measured at the quarter thickness location (T/4) of thick parts (300 mm) are representative of the mechanical properties of the zone located between quarter and three-quarter thickness of the product, and in particular of the mid part section. The mechanical properties change rapidly between the surface and the quarter thickness location. Thus the temperatures which are characteristic of the position of the ductile-to-brittle zone are near the surface location lower than at the T/4 location. This is generally not considered when evaluating embrittlement induced by neutron irradiation, but is in fact an additional safety margin.

Microstructural observations showed that the forged SA508 Cl3 material had a uniform microstructure throughout, i.e. the percentage

of bainite remains constant. However, sulphide stringers appear throughout the forging and appear to have formed in large clusters. These clusters are, however, 'broken-up' at the surface of the SA508 C.3 steel nozzle as a result of the forging process (Plates 5.15 - 5.17).

6.1.2 Metallurgical structures encountered in thick products in Mn-Ni-Mo low alloy steels

Typical thicknesses range from 250 mm to 460 mm for reactor vessel forgings and reach 600 mm for the tube plate of the steam generator in the as quenched geometry.

The cooling rates at 700 °C encountered through-thickness of the different finished parts are located from 8000 °C/hr at the final machined surface to 600 °C/hr at the mid-thickness of the tube plate (Fig. 6.2).

The CCT diagram (Fig. 6.3) shows that under these conditions, a duplex microstructure is encountered which basically consists of bainite with a small amount of ferrite. The proportion of ferrite is generally under 20% at $^{1}/_{4}T$ location and may reach 40 - 50% at mid-thickness for the thickest products (Fig. 6.4).

The tempering temperature is selected to optimize the balance between tensile mechanical properties and toughness. In particular, tempering at an excessively high temperature results in degradation of the impact resistance due to the irreversible temper embrittlement of the material.

For the 270 mm thick nozzle section, no through-thickness effects were noticed, both microstructurally and mechanically (using the hardness test as the criterion). Clearly the mechanical properties will be more adversely affected by the presence of MnS stringer inclusions (as observed for the fatigue tests).

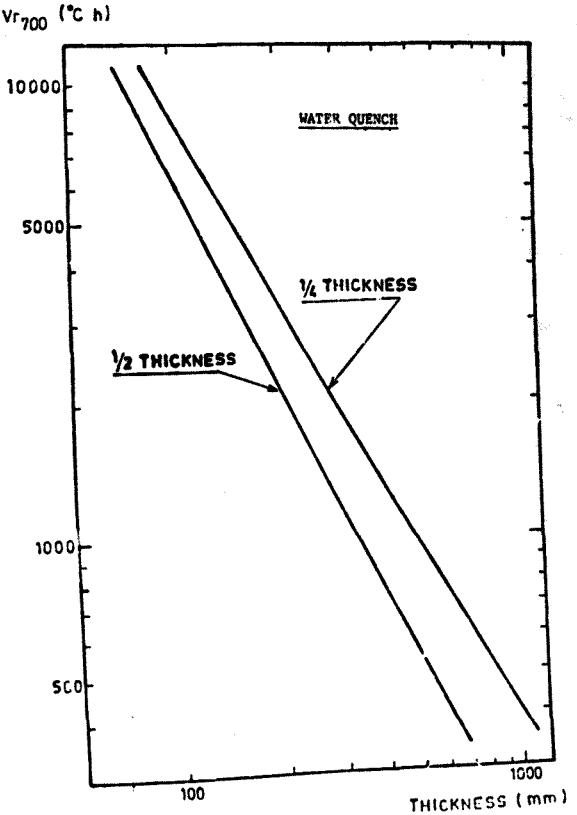

FIGURE 6.2: Cooling rate at 700 °C/h as a function of thickness

A508 Cl. 3 A 533 gr.B Cl.1	Grain ℵ 9.10	Austenitizing 900°C - 1h

C	S	P	Si	Mn	Ni	Co	Cr	Mo	Cu	Al
0,18	0,006	0,010	0,26	1,21	0,69	0,016	0,27	0,48	0,11	0,035

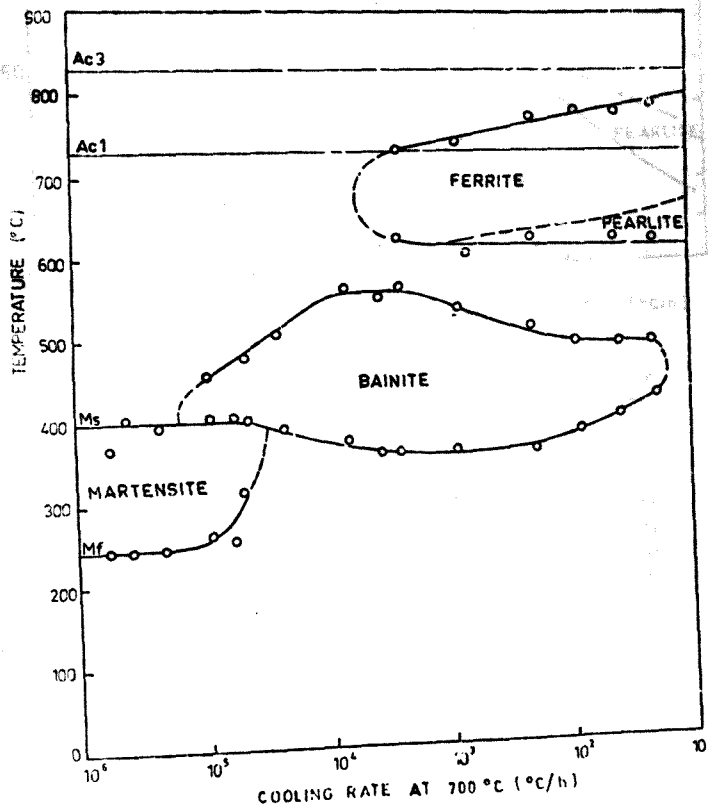

FIGURE 6.3: Continuous cooling transformation diagram

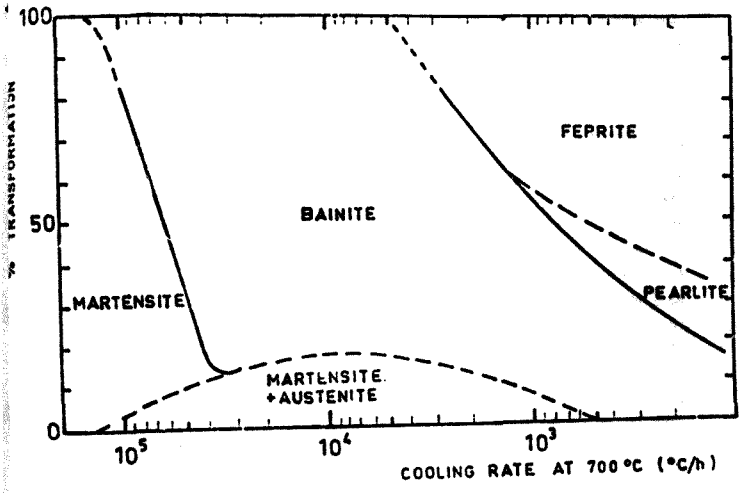

FIGURE 6.4: Microstructure developed as a function of cooling rate (SA508 C.3, austenitizing 900 °C/hr, Grain size: 9-10)

6.2 Sample Potential Monitoring

Until the present time much controversy has been attached to the necessity for compact tension specimen isolation from the clevis and pin arrangement. It has been argued that specimens contacting clevises (usually manufactured from more corrosion resisti.; materials, in the P.W.R. environment) could result in a galvanic effect which could interfere with the corrosion-fatigue process. Also, the pins are often not manufactured from the same material as the clevis and might need to be isolated from the specimen. In certain overseas laboratories (e.g. Harwell), zirconia washers and sleeves are used to isolate electrically the specimen from the pins and clevises. This electrical isolation relies on the extremely low

conductivity of the oxide layer, formed on zirconium, after a special furnace heat treatment. It has, however, been observed that this brittle oxide layer 'peals' off and, after only a few tests, electrical isolation is broken [53].

It was therefore thought that a simple potential monitoring test (during corrosion fatigue) followed by a potentiodynamic test for both SA508 C.3 and stainless steel (316), the clevis material, would prove whether specimen isolation was necessary. Figure 5.3E shows quite clearly that the sample potential (monitoring) corresponds to E_{corr} (the freely corroding potential) determined in a potentiodynamic test. It was found that for a probe mounted 1 cm from the crack initiation point (i.e. 1 cm from the specimen side face) the sample potential only varied with test temperature. An E_{corr} of -376 mV (S.C.E.) for the clevis material in a P.W.R. environment shows that the presence of 316 stainless steel, being electrically connected to the sample, has had no effect on the corrosion potential of the compact tension specimen. It can therefore be concluded that specimen isolation is not essential.

Clearly, the above conclusion is only valid for the system used during this series of tests. One could assume that if E_{corr}(clevis) >> E_{corr} (C.T. specimen) (at the temperature of testing) and if the sample potential corresponds closely to E_{corr} for the specimen (in the P.W.R. environment), then electrical isolation would not be required. Certainly, for SA508 C.3 and SA533 Gr B steels, the above conditions would usually be met.

It should also be pointed out that the reactor pressure vessel material is in contact with the cladding material, typically 304 type stainless steel or Inconel 600, in the R.P.V. Therefore, it is considered unnecessary to isolate the compact tension specimen for the clevis and pin arrangement.

6.2.1 Pourbaix diagram - Fe - H_2O system

One of the most useful developments of recent years has been the construction of diagrams, with pH and potential as co-ordinates, representing the various chemical and electrochemical equilibria which affect metallic corrosion. The curves divide the diagram into regions within which immunity, corrosion or passivation may be expected to prevail [52].

Figure 6.5 shows the Pourbaix diagram for iron at 25 °C. This diagram can also be used for the low alloy SA508 C.3 steel without incurring too much error.

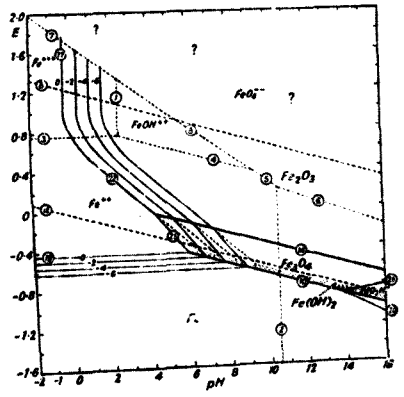

FIGURE 6.5: Pourbaix Diagram for Iron at 25 °C

The sample potential values for SA508 C.3 steel were found to be -674 mV (S.C.E.) at 20 °C and -649 mV (S.C.E.) at 50 °C. These E_{corr} potentials were measured at a pH of 6.5. Simplifying the above Pourbaix diagram in the curve below and showing the regions of corrosion, passivation and immunity result in Fig. 6.6, for iron.

6.2.1 Pourbaix diagram - Fe - H_2O system

One of the most useful developments of recent years has been the construction of diagrams, with pH and potential as co-ordinates, representing the various chemical and electrochemical equilibria which affect metallic corrosion. The curves divide the diagram into regions within which immunity, corrosion or passivation may be expected to prevail [52].

Figure 6.5 shows the Pourbaix diagram for iron at 25 °C. This diagram can also be used for the low alloy SA508 Cl3 steel without incurring too much error.

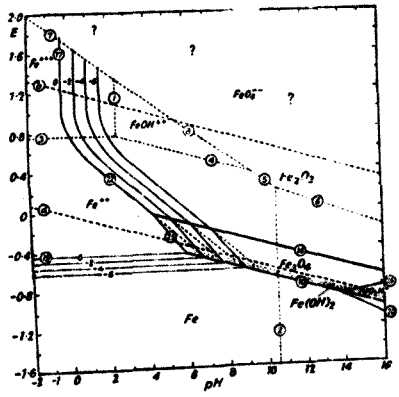

FIGURE 6.5: Pourbaix Diagram for Iron at 25 °C

The sample potential values for SA508 Cl3 steel were found to be -674 mV (S.C.E.) at 20 °C and -649 mV (S.C.E.) at 50 °C. These E_{corr} potentials were measured at a pH of 6.5. Simplifying the above Pourbaix diagram in the curve below and showing the regions of corrosion, passivation and immunity result in Fig. 6.6, for iron.

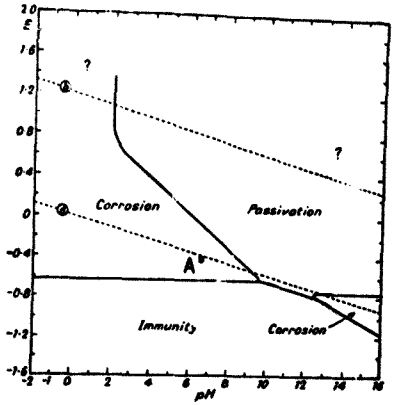

FIGURE 6.6: Simplified Pourbaix Diagram for iron (25 °C)

Note that the regions of corrosion, passivation and immunity change with temperature and Fig. 6.7 shows the above diagram at 300 °C. However, assuming that the Pourbaix diagram does not change much for temperatures in the range 20 to 50 °C and scaling the sample potential values to correspond to the standard hydrogen electrode, the C.T. specimen potentials can be superimposed on Fig. 6.6. The two potential values -428 mV (20 °C) [57] and -426 mV (50 °C) [57] correspond to point A in Fig. 6.6. Clearly, the conditions lie within the corrosion region, i.e. from a thermodynamic point of view the SA508 Cl.3 material corrodes at the test conditions.

Clearly, this corrosion region shrinks as the temperature increases and for 300 °C testing (for similar pH and potentials) the Pourbaix diagram shows that the Fe_3O_4 oxide regime (passivation) could define the test system. Potentials of typically -700 mV (S.H.E.) have been reported for 288 °C testing in P.W.R. environments [54].

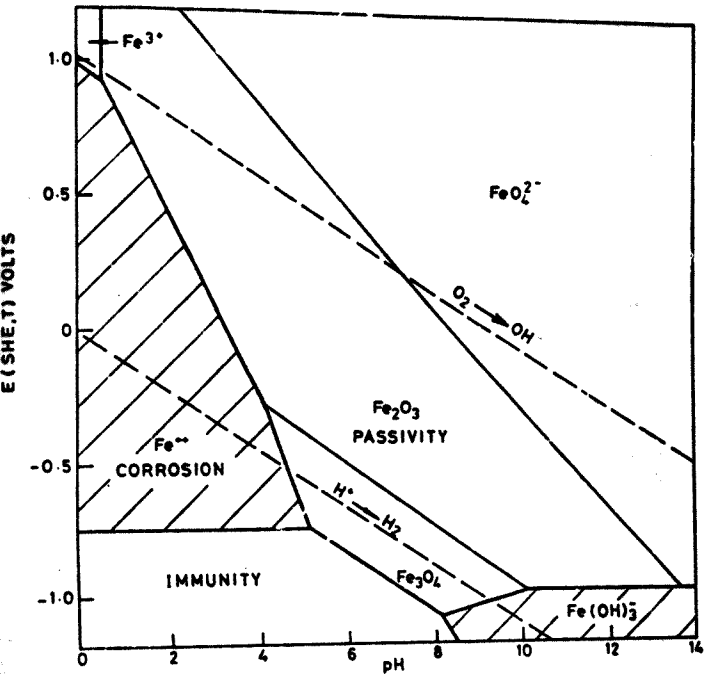

FIGURE 6.7: Pourbaix diagram for iron in water at 300 °C (dissolved iron 10^{-5} M)

Anodic dissolution and hydrogen embrittlement processes could both aid in producing environmentally enhanced crack growth.

The da/dN versus ΔK curves have clearly shown that crack growth rates are higher in P.W.R. environments (as opposed to air testing) at R-ratios of 0.2. One could argue that the enhanced crack growth rates are as a result of the presence of inclusions (ex. for R = 0.7), but this cannot explain why crack growth rates in P.W.R. environments are faster than crack growth rates in air environments when fractographic evidence shows that both air and P.W.R. test steels have similar inclusion contents (size, shape and morphology of inclusions are also similar). Certain regions of fast crack growth (Plate 5.54) were (only observed during S.E.M. analysis on the P.W.R. test fracture surfaces) found before the inclusion. This is clearly evidence for a hydrogen embrittlement crack growth assisted mechanism. It should be remembered that the P.W.R. simulated water has extremely low oxygen contents (less than 10 ppb) but, is saturated with a hydrogen over pressure of up to 40 kPa. This corresponds to a dissolved hydrogen content of up to 21.7 std. cc/kg H_2O. Clearly, the conditions for having a hydrogen embrittlement process are met and would appear that inclusions also play a rôle in the embrittlement process. An anodic dissolution mechanism for environment assisted crack growth can, however, not be ruled out (see page 236).

6.3 Sulphide Inclusions

MnS as a inclusion is easily recognized in the optical microscope. It is a dove-grey in colour, plastic, slightly transparent and inactive in polarized light (plate 5.5). Deformation of the steel usually results in the MnS-phase being elongated in the working direction, forming stringers or plates. The morphology of MnS in steel ingots depends on the steelmaking practice. Using the classification given by Sims and Dahle [51], the sulphide phase may be described as a Type I, Type II or Type III.

Type I is globular with a wide range of sizes, often duplex with oxygen compounds and with an apparently random distribution. This type is found in both carbon and low alloyed steels.

MnS of Type II has a dendritic structure and is often called grain-boundary sulphide because it is distributed as chainlike formations or thin precipitates in primary ingot grain boundaries. Sometimes it seems to have solidified in an eutectic pattern. This type is found in steels, deoxidized with Al without an excess of the deoxidizing metal.

Type III is irregular, often angular in shape and randomly distributed in the matrix. This type is often similar to Type I and there is no marked difference between the two types. However, Type III always forms monophase inclusions, whereas Type I usually is present in multiphase inclusions. Type III is most frequently found in steels deoxidized with an excess of Al.

The sulphides observed in this work can therefore be assumed to be Type II inclusions which are found in killed steels, thoroughly deoxidized with Al, but without excess and where the oxygen content is low. As a consequence these steels have a high sulphur solubility and the sulphide phase precipitates late in the last parts of the steel ingot to solidify. Therefore, the Type II sulphide is found in the primary grain boundaries in a dendritic, eutectic pattern. The precipitation pattern for Type II sulphide depends more on temperature and oxygen content of the steel than for Type I sulphides, which are precipitated at higher temperatures and oxygen contents.

Optical microscopy, macroscopy, sulphur printing and scanning electron microscopy of the fracture surfaces show clearly that the sulphide orientation is that shown in Figs 5.2 and 5.3. The sulphides lie in the dark bands (Plate 5.2) which would appear to be segregated regions. The formation of these stringer type inclusions is as a result of the hot forging and steel making process.

Sulphur printing and macroscopy shows that large clusters of stringer sulphides are present throughout the forged SA508 C.3 material. Probably one of the most important observations is that the sulphides do not lie normal to the through-thickness direction,

MnS of Type II has a dendritic structure and is often called grain-boundary sulphide because it is distributed as chainlike formations or thin precipitates in primary ingot grain boundaries. Sometimes it seems to have solidified in an eutectic pattern. This type is found in steels, deoxidized with Al without an excess of the deoxidizing metal.

Type III is irregular, often angular in shape and randomly distributed in the matrix. This type is often similar to Type I and there is no marked difference between the two types. However, Type III always forms monophase inclusions, whereas Type I usually is present in multiphase inclusions. Type III is most frequently found in steels deoxidized with an excess of Al.

The sulphides observed in this work can therefore be assumed to be Type II inclusions which are found in killed steels, thoroughly deoxidized with Al, but without excess and where the oxygen content is low. As a consequence these steels have a high sulphur solubility and the sulphide phase precipitates late in the last parts of the steel ingot to solidify. Therefore, the Type II sulphide is found in the primary grain boundaries in a dendritic, eutectic pattern. The precipitation pattern for Type II sulphide depends more on temperature and oxygen content of the steel than for Type I sulphides, which are precipitated at higher temperatures and oxygen contents.

Optical microscopy, macroscopy, sulphur printing and scanning electron microscopy of the fracture surfaces show clearly that the sulphide orientation is that shown in Figs 5.2 and 5.3. The sulphides lie in the dark bands (Plate 5.2) which would appear to be segregated regions. The formation of these stringer type inclusions is as a result of the hot forging and steel making process.

Sulphur printing and macroscopy shows that large clusters of stringer sulphides are present throughout the forged SA508 Cl.3 material. Probably one of the most important observations is that the sulphides do not lie normal to the through-thickness direction,

but rather at 10^0 to normal. This means that bands of sulphides do intersect the inside surface of the pressure vessel nozzle. Clearly these regions (Plate 5.9) could act as crack initiating sites for corrosion fatigue or stress corrosion cracking (notch effect). Plates 5.15 and 5.17 do show that the sulphides are less clustered at the surface, and that the density of sulphides is greater, clearly as a result of the forging process. Both these plates do show the 10^0 angle that the sulphides make with the inner wall of the nozzle. EDAX analysis showed all sulphides on the fatigue fracture surface to be MnS (Plate 5.21).

An important observation to make is that the sulphides clearly affect crack growth in a dramatic way (see possible mechanisms) and neither of the heat treatments (rough or quality heat treatments) will affect the sulphide size, shape or morphology.

6.4 CRACK GROWTH RATE DATA (A mechanistic approach)

Clearly, two possible effects need to be considered when discussing the fatigue crack growth rates for the SA508 C.3 steel forging. Firstly, inclusions can be seen to aid crack growth without the effect of a P.W.R. environment. Secondly, hydrogen embrittlement and anodic dissolution processes aid in the crack advancement, but this can only be deduced once careful attention has been given to the inclusion clusters found on the fracture surfaces.

6.4.1 Air tests

Figure 5.7 shows that decreasing the frequency of fatigue cycling, in an air environment, has had little effect on the fatigue crack growth rate of SA508 C.3 steel. Fractographic evidence shows that both air tests have few MnS inclusions on the fracture surfaces and that these inclusions do not cause subsequent regions of fast crack growth. Rather, ductile striation crack growth is the mechanism whereby the crack has propagated through the steel specimen. Thus, for similar crack growth mechanisms and approximately similar sul-

phide inclusion volume fractions, it would be expected that crack growth rates would be similar for the 1 Hz and 10 Hz tests (crack growth along orientation A).

Figure 5.12, on the other hand, shows that test AIR(40R) produces crack growth rates well above those experienced in the above tests. The air line data for test AIR(40R) even lies above the ASME XI (1980) subsurface flaw (air) curve. This is however not surprising when the fractographs are studied. Long manganese sulphide inclusions can be seen to initiate rapid crack growth. The MnS inclusions affect the local stress field ahead of the crack tip since the Mn^{+} in matrix bonding is weak and the interfaces probably separate at low tensile stresses (probably before the elastic limit is reached). Therefore, the strain is concentrated in the adjacent matrix, the MnS really acting as a stress concentrator. Plate 5 32 clearly shows a pronounced terrace effect. These regions (base of terrace) would be located away from the main crack path and are joined to the main fracture surface by ductile tearing.

The air test corresponding to a 0.7 R-ratio (Fig. 5.26) can be seen to produce crack growth rates above those predicted by the ASME air line. Once again the fast crack growth rates can be seen to result from the presence of large MnS stringer inclusions.

It is also important to note that the general fracture surface consists of large regions of fast fan-shaped crack growth. Plate 5.68 shows this fan-shaped crack growth occurring after the crack front has passed a MnS. This could be explained by crack velocities, i.e. before the crack reaches the MnS the growth mechanism is ductile striated growth. When the crack front reaches the inclusion, the local crack growth rate is accelerated and only slows down once the effect of the inclusion has been dissipated; this period corresponding to fast ductile striated crack growth.

Clearly, the two orientations chosen for crack growth studies are the 'best' and 'worst'. In other words, the best results, i.e. low

crack growth rates, would be obtained with crack growth normal to the direction of the sulphides. Samples in orientation B were found to give rise to crack growth in a direction parallel to the manganese sulphides. Microscopy and sulphur printing revealed that the clusters of MnS inclusions (Plates 5.12 and 5.13) lie in the notch direction of specimens machined from orientation B (Fig. 4.2).

6.4.2 P.W.R. environment corrosion fatigue tests

The 'basis' tests P.W.R. (1a) and P.W.R. (1b) both showed crack growth rates above that found for the air line test AIR(3), although the inclusion concentration present on the fracture surface for all three tests was approximately the same. Plates 5.25 and 5.30 show regions of fast crack growth before the crack reaches the inclusion. A region of ductile tearing appears just before the inclusions, this area corresponding to crack movement towards the inclusion, i.e. not normal to the stresses.

Some inclusions have originated rapid crack growth regions (Plates 5.24, 5.26, 5.27, 5.29 and 5.30). As both tests, P.W.R. (1a) and P.W.R. (1b), show similar fractographic features, it can be assumed that hydrogen embrittlement is influencing crack growth. The lower the test frequency, the greater the environmental effect (higher crack growth rates). This is indeed what one would expect if hydrogen embrittlement and anodic dissolution were assisting crack growth, since lower frequencies allow more time for both hydrogen diffusion ahead of the crack tip and anodic dissolution at the crack tip. Fast failure regions are apparent about the manganese sulphides because sulphide inclusions could act as preferential 'hydrogen trap sites'. The non-coherent interface between the MnS and the 'iron' matrix would create large vacancy regions where hydrogen could accumulate.

As crack growth, via an environmentally assisted fan-shape mechanism, is always in the direction towards the MnS, it could be concluded that hydrogen embrittled areas are particularly prominent about the MnS. Obviously hydrogen has diffused preferentially to

the MnS inclusion. This would dispel the gas pressure bursting theory for these tests. According to this theory hydrogen accumulation at sites ahead of the crack front could be high enough to cause failure about the accumulation site. This would show-up fractographically as a crack initiating from the inclusion and travelling back towards the advancing crack front. However, for 1 Hz and 10 Hz tests, the hydrogen accummulation at a manganese sulphide would not be all that great, before the advancing crack had reached the inclusion.

Note that the inclusion sites are often associated with branched cracks. These are cracks that have formed at the 'base' of the inclusion. These regions would probably be more heavily embrittled and the main crack front would therefore follow the embrittled path. Only once the tensile stress component had 'out-weighed' this embrittlement effect, would the crack continue normal to the tensile stress, i.e. restart from the inclusion site.

6.4.2.1 **Influence of sulphide orientation**

The MnS inclusions lie parallel with the crack growth rate directions and it would be expected that crack growth rates should be higher for the orientation specimens than through-thickness orientated specimens (for the same mechanical testing conditions). This was found for both test P.W.R. (2a) and P.W.R. (2b) but, it was observed that the crack growth rates for the two frequency tests (10 Hz and 1 Hz) gave similar crack growth rates (Fig. 5.19).

The reason for the above behaviour is immediately obvious on comparison of the fractographs (Plates 5.36 - 5.52). The fractography for specimen P.W.R. (2a) shows large MnS stringers extending across large regions of the fracture surface. These stringers have resulted in rapid crack growth rates and correspondingly flat, more brittle fracture surfaces than those observed for specimen P.W.R. (1a). Both 'whole' and 'broken-up' MnS (Plates 5.39 - 5.45) inclusions have produced large fan-shaped regions corresponding to environmentally assisted failure. Plate 5.39 shows a typical chevron

pattern between the long MnS stringers. The MnS inclusions occur in discontinuous stringers and for large sections, the crack passes from the 'tail' of one inclusion to the 'head' of another, thus facilitating rapid crack growth.

Specimen P.W.P. (2b) shows a similar 'flat' fracture surface (still ductile striated crack growth), but the number of inclusions found on the surface is considerably reduced. The inclusions are also more globular, and in some cases are flat disk-like inclusions (possibly Type I MnS inclusions; see Plate 5.52). Therefore, although the hydrogen embrittlement/anodic dissolution assisted crack growth model is still valid, the presence of inclusions has resulted in even greater crack growth rates. Note, comparing tests P.W.R. (1a), (1b), (2a) and (2b) with the respective air line data one could make the following deduction: For test P.W.R. (2a) the presence of a larger concentration of manganese sulphides has resulted in a crack growth rate increase of approximately twice that expected if only hydrogen embrittlement/anodic dissolution has assisted crack growth (with only a few MnS inclusions present).

6.4.2.2 Effect of temperature variation

Since hydrogen embrittlement and anodic dissolution have been identified as the environmental factors enhancing crack growth, it would be expected that increasing the testing temperature (50 °C) should increase the crack growth rates above those found for the 20 °C tests. Increases in temperature should result in more rapid hydrogen diffusion and metal dissolution, but the MnS inclusion network would also need to be considered since, if very few MnS inclusions were found to assist crack growth, the increase in temperature could actually decrease the crack growth rates.

Figure 5.22 shows that both the 10 Hz and 1 Hz tests exhibit advanced crack growth above the air line data. A frequency effect is also noted, in that the lower frequency test (1 Hz) shows greater crack growth rates than the 10 Hz test over the entire ΔK range tested.

On comparing the 50 °C tests with the 'corresponding' 20 °C tests, it was found that the 10 Hz test showed a greater increase in crack growth rate. This could be expected from the fractographic evidence, since regions of 'fast'-ductile-striation crack growth are evident (Plate 5.53). Plate 5.54 shows a region of brittle cleavage before the crack has encountered the MnS stringer. This region is about 25 μm long. The inclusions appear to be sites that have initiated fan-shaped regions of environmentally assisted crack growth (Plates 5.56, 5.57 and 5.59). Plate 5.58 shows a region of brittle cleavage found after the crack front has reached the MnS. The regions of cleavage are linked together by ductile tearing. A similar region of cleavage can be seen in Plate 5.59. P.W.R. (3b) (1 Hz test) shows that the inclusions have initiated regions of fast crack growth. The majority of inclusions lie below the crack path. This has resulted in a terraced appearance where the crack has had to grow 'down' to the MnS. The base of the inclusion site is usually an initiator for a crack (this has been explained before). A fanned region of environmentally assisted crack growth then emanates from the inclusion site (Plates 5.61 and 5.62).

6.4.2.3 R-ratio tests

The 0.7 R-ratio air test has already been discussed and the rapid growth rates observed were ascribed to the inclusion clusters found on the fracture surfaces, resulting in a rapid ductile striation mechanism of crack advance.

The P.W.R. environment tests show an inverted behaviour, in that the plateau formation changes to a linear (log scale) increase in crack growth rate with increasing ΔK, for the 10 Hz test. The opposite effect was found for the 1 Hz test. It is important to note that the results of both tests lie above the air line data and indeed, this could be expected, since hydrogen embrittlement and anodic dissolution would be easier at high R-ratios. The reason is that the maximum stress (25 kN) remains constant for both the 0.2 R-ratio and 0.7 R-ratio tests and therefore, the minimum loads vary (5 kN and 17.5 kN respectively). The 0.7 R-ratio is therefore

permanently in a 'higher' tensile stressed state, which would promote hydrogen diffusion and increase the effectiveness of hydrogen adsorption. Likewise, the stress concentrating effect brought about by dissolution at slip step emergence would be enhanced.

Test P.W.R. (4a) resulted in an initial ductile striation crack advancement process but, at $\Delta K = \pm 15$ MPa $\sqrt{m}$ cleavage facets were observed (Plates 5.73 to 5.75) and a small region of intergranular failure occurred. As both specimens, P.W.R. (4a) and (4b) showed these features at approximately the same ΔK, and were cut from the same section of material, it can be assumed that these regions are heavily segregated. This, in itself, could cause the fractographic features, but hydrogen embrittlement could certainly have contributed to the intergranular cracking. For $\Delta K > 15$ MPa $\sqrt{m}$ inclusions were found to influence crack growth (a) fan-shaped regions of environmentally assisted crack growth after the inclusions (Plate 5.76); (b) fan originating from an inclusion site (Plate 5.77); (c) 'fast'-ductile-striated growth related to an inclusion (Plate 5.78).

Test P.W.R. (4b) shows crack growth as regions of ductile striation crack advancement for $\Delta K < 15$ MPa $\sqrt{m}$. Inclusions were observed for $\Delta K > 15$ MPa $\sqrt{m}$ but their effect on the ductile striation crack growth advancement process was only local (i.e. small regions of fast crack growth ahead of the inclusion).

6.5 CRACK GROWTH MECHANISMS

The experimental work carried out above does not clearly differentiate between hydrogen embrittlement and anodic dissolution methods for advanced crack growth. The oxide rupture mechanism is, however, ruled out since the oxide formed on SA 508 C.3 material, at the temperatures of interest, is not a true passivating oxide layer. This does not apply to high temperature testing where a passive oxide layer is formed (see page 227).

The MnS inclusion morphology on the fracture surface must, however, also be accounted for. Whenever significant enhacement occurs, the

ductile striation mechanism changes to regions of relatively fast ductile crack growth, or the presence of sulphide inclusions has played a role in crack advancement. Fan shaped features would indicate that MnS inclusions have a definite role in the enivronment assisted crack growth process (Plates 5.57 and 5.6d). This is enhanced by the discovery of regions of fast failure in front of the MnS inclusions (Plate 5.54). It is also shown that the inclusions are associated with localized microcracking at the 'base' of the inclusion site. The manganese sulphides have been seen to be associated with a 'terraced' fracture surface, whereby the crack has grown by ductile cleavage (Plates 5.61 and 5.62) towards the inclusion, in preference to normal to the tensile fatigue load. Fast fan-shaped crack growth links the terraces with the main crack front. Less inclusions have been found in the ductile striation fracture morphologies.

The MnS inclusions may conceptually play two rôles in the crack advancement process. First they can trap hydrogen entering the metal lattice when hydrogen diffuses towards the area of maximum hydrostatic stress ahead of the crack tip. The elongated inclusions, acting like microcracks, produce an intense stress-strain distribution around themselves as they are enveloped by the plastic zone. Trapped hydrogen and the microcrack-type behaviour of the elongated inclusions together with the high tensile stresses ahead of the fatigue crack tip, can trigger the hydrogen-induced cracking found around inclusions. Hydrogen embrittled regions before the MnS can cause rapid crack advancement to the MnS. These embrittled regions correspond to prior hydrogen diffusion paths. The resulting crack front path is seen as a terrace formation, where inclusions displaced from the main crack path are connected to the fracture surface by ductile tearing. The terraces are mainly observed at high ΔK levels and their presence indicates that they provide preferential crack growth paths for crack propagation.

The two principal processes proposed to control the environmentally assisted cracking of SA 508 Cl3 pressure vessel steel in a simulated P.W.R. environment are: (i) metal loss by anodic dissolution at

the crack tip giving rise to crack advance at a rate controlled by the kinetics of the various electrochemical reactions and loading conditions and (ii) adsorption phenomena (hydrogen embrittlement) at the crack tip and associated diffusion into the strained lattice ahead of the crack resulting in a decrease in local mechanical integrity. Adsorption phenomena include concepts of reduction in surface energy brought about by chemisorption of specific environmental species which, in the case of hydrogen atoms, can absorb into the strained crack tip. Both adsorption and dissolution processes have been used in mechanistic descriptions of crack initiation and growth with each contributing to various extents at different states of crack development. The dominant mechanism is that which results in the fastest crack development with overall kinetics conforming to that specific underlying process. Removal or reduction of one essential component may stop cracking by this process but does not preclude the possibility of cracking continuing by another. It is important to realize that corrosion fatigue phenomena are a part of general materials behaviour occurring over ranges of conditions, not a consequence of a unique set of chance circumstances. As such, the assumption of a unique mechanism or process for even a single alloy/environment system is considered unrealistic.

All proposed mechanisms for the environmental enhancement of crack growth include a direct interaction of the environment with the straining metal at the tip of the advancing crack. Thus, any analysis of the crack advance process should include a description of this crack tip region, both within the aqueous solution and in the strained metal.

The use of fractography studies in the development of mechanistic understanding of growth processes has introduced much controversy. This is a consequence of the observation that in ductile materials where slip enhanced anodic dissolution models are proposed, there is rarely any fractographic evidence for either significant slip or anodic dissolution. It might be argued, however, that dissolution occurs only over a very narrow crack front, perhaps only a fraction

of a nonometer, as a consequence of the restrictions imposed by factors such as chemical segregation or lattice strain distortion at dislocations and grain boundaries. Such considerations, however, have still to be reconciled with other experimental data which suggests more electrochemical activity than would result from such highly localized dissolution, particularly the evolution of large quantities of cathodically produced hydrogen and significant composition changes in crack solution chemistry.

Corrosion fatigue crack growth will occur at persistent slip bands which are preferentially attacked leading the stress intensification. Corrosion as well as local mechanical deformation results in the formation of numerous slip bands which act as microcrack initiation/growth sites. The corrosion presumably occurs because metal atoms associated with mobile dislocations in the persistent slip bands are more active than surrounding slip bands, leading to strain relief in the surface and significant increases in surface deformation. The electrochemical attack occurs at plastically deformed areas of metal, with non-deformed metal acting as the cathode. The cathodic half cell reaction could involve the production of hydrogen.

Hydrogen embrittlement can also be aiding crack growth where only a few inclusions are present. Hydrogen adsorption and limited hydrogen absorption at the crack tip could facilitate mechanical separation of the steel matrix. It is important to realize that hydrogen embrittlement and/or anodic dissolution do not need to result in a change in fracture surface features, but its effect can clearly be seen in the da/dN versus ΔK curves, i.e. increased fatigue crack growth rates.

The P.W.R. environment tests therefore show three complementary mechanisms for crack advance:

1) Mechanical fatigue crack growth (applicable to air tests).

2) Corrosion fatigue crack growth by a hydrogen embrittlement mechanism (adsorption at the crack tip or diffusion ahead of the crack tip).

3) Corrosion fatigue crack growth by the anodic dissolution mechanism (corrosion at active metal sites of slip emergence).

Clearly, the presence of manganese sulphide inclusions can aid either or both of process (1) or (2). Firstly, by acting as stress concentrators ahead of the crack front, the inclusions can assist in the mechanical fatigue crack growth, and secondly, by acting as hydrogen trap sites resulting in preferential embrittled path ways to the MnS inclusions (in the 'vicinity' of the crack front). MnS orientated parallel with the crack growth direction will aid fatigue crack growth more than MnS inclusions orientated normal to the crack growth direction. This can be explained by the greater stress concentrating effect of the former inclusion and by the fact that the crack has effectively been advanced by the length of the inclusion (non-coherent). Clearly, if the inclusion lies parallel to the crack front (Type II MnS stringer), the crack will advance by the length dimension which is always much greater than the width of the inclusion (typically 50 : 1).

6.6 GENERAL

Clearly the corrosion fatigue of SA508 Cl3 steel in simulated P.W.R. environments or air must be discussed with reference to MnS inclusion distributions and rigorous testing parameter description. Testing parameters should include: mechanical testing parameters (frequency, waveform, R-ratio, maximum load, constant stress or constant ΔK), water chemistry (pH, conductivity, oxygen levels, dissolved hydrogen, Cl^-; F^-; SO_4^{2-}, B, Li), test conditions (sample description, specimen isolation, potential monitoring etc.). A detailed metallurgical investigation is also necessary to characterize the base SA508 Cl3 steel forging. Clearly, if any of the above factors is omitted, no confidence can be placed in the results.

It is obvious from the above discussion that one cannot discuss corrosion fatigue data without discussing the effect that inclusions (MnS) are likely to have on crack assisted growth. An important practical conclusion is that 'modern' steel, which generally contains low contents of small spheroidal manganese sulphides, should be less susceptible to environment-assisted cyclic cracking than other steels, which contain amounts of manganese sulphide in stringer form. In addition, quoting bulk sulphur contents in these steels is 'useless' information, unless a detailed analysis is given of the sulphide size, shape, distribution and morphology in the steel forging, since low sulphur steels (containing MnS stringers) could give higher crack growth rates than high sulphur steels having small spheroidal MnS inclusions.

An important feature of the corrosion fatigue tests is the scatter that would be likely to arise for exactly the same test conditions. This scatter would depend largely on the position at which the C.T. specimen had been extracted, with respect to the main forging. One could envisage a C.T. specimen orientated with the notch and later fracture surface lying along the MnS bands shown in Plate 5.12. It would be expected that crack growth rates, for this hypothetical case, (for an air test) would lie above the ASME XI (1980) wet line data. These MnS stringers could act as initiating sites for corrosion fatigue and it would be expected that a crack would initiate at the MnS-matrix interface. The interface is mechanically 'weak' and can act as a rapid hydrogen diffusion path. This is important when one considers that the sulphide stringers (Plates 5.9 - 5.11) could emerge at the nuclear pressure vessel inside wall.

It would therefore appear that the corrosion fatigue crack growth will depend, to a certain extent, on where the specimen is notched with respect to the inclusions. Thus, scatter that would appear in results (for nominally the same testing conditions) is a real phenomenon. Fractographic results could indicate that the scatter in the observed cyclic crack growth rates is consistent with the fractographic appearance and therefore is real.

As tests AIR(40R) and AIR(2) both lie above the ASME XI (1980) AIR crack growth rate curve, it can be assumed that the ASME AIR line curve does not represent an upper bound on crack growth rates for this steel. Clearly, codes such as the ASME codes will need to include information on: material characterization (i.e. not just chemical compositions and properties of the steels, but also information on segregation effects, sulphide stringers etc.) and test environment characterization (including water chemistry particulars, specimen potentials etc.).

7.0 CONCLUSIONS

7.1 Material Testing

1. Charpy tests, optical microscopy, sulphur printing, macroscopy, corrosion fatigue tests and S.E.M. studies have shown that large clusters of MnS inclusions are present in the wrought SA508 CA3 steel. These inclusions give rise to anisotropic behaviour, i.e. low impact values and high crack growth rates for specimens in which crack growth takes place parallel to the MnS (Type II) stringers. No orientation effect was observed in the tensile and hardness tests.

2. Chemical analysis showed the reactor pressure vessel steel to be a low alloy carbon steel and no through-thickness compositional variations were observed. The microstructure was upper bainite with less than 5% ferrite. No microstructural through-thickness variations were observed. Sulphide inclusion clusters appear at various through-thickness regions and only at the surface of the forging are the inclusion clusters 'small', but the density of inclusions is considerable. The inclusions do not lie normal to the surface, but rather at an approximate angle of 10^0. Therefore, the inclusion clusters intersect the surface of the forging. These regions could act as initiation sites for corrosion fatigue or stress corrosion cracking.

3. C.T. specimen potential monitoring has shown conclusively that, for the testing system described, no sample isolation from the clevis and pin arrangement is required. The sample potentials recorded correspond directly to the free corrosion potential for the SA508 CA3 steel determined during potentiodynamic tests. The sample potentials only vary with testing temperature.

4. pH and potential monitoring have shown, using a Pourbaix diagram, that the SA508 CA3 pressure vessel steel does corrode (i.e. no immunity or passivation). This indicates that corro-

sion assisted fatigue could result from a hydrogen embrittlement mechanism as well as an anodic dissolution mechanism. It is quite feasible that both processes complement one another to provide the environmentally enhanced fatigue crack growth observed.

5. Corrosion fatigue tests in air showed that the orientation specimen and the 0.7 R-ratio air test gave crack growth rates greater than those predicted by the ASME XI (1980) dry (air) line for subsurface flaws! Clearly, revision of the codes is required.

6. Corrosion fatigue testing in a P.W.R. environment (0.2 R-ratio) showed that environmental enhancement of the crack growth rate was observed for both 10 Hz and 1 Hz tests. The 1 Hz tests produced the largest increase in crack growth rates when referenced to the air line data. Increasing the test temperature from 20 °C to 50 °C increased the crack growth rates (for similar tests) marginally. Orientation tests (crack growth parallel to the MnS stringer inclusions) showed much larger crack growth rates than the through-thickness crack growth specimens. This was seen to be the result of the presence of the MnS stringers aiding fast fan shaped crack growth. The effect of R-ratio can be seen to shift the da/dN versus ΔK curves to lower values of ΔK and da/dN. Testing at two frequencies (1 Hz and 10 Hz) gave an inverse crack growth relationship which can be related to fractographic features. In general, all da/dN versus ΔK curves showed increases in ΔK for increases in crack growth rates. Only the R-ratio P.W.R. environment tests showed a plateau behaviour (plateau at low ΔK for the 10 Hz test and plateau at high ΔK for the 1 Hz test).

7. The mechanism of crack growth is related to the MnS inclusions (size, shape, distribution and morphology) found on the fracture surfaces and to anodic dissolution/hydrogen embrittlement. The P.W.R. water being saturated with hydrogen which could embrittle the pressure vessel steel through adsorption at the

crack tip or diffusion ahead of the crack tip, which would result in embrittled hydrogen diffusion paths. The MnS inclusions act as trap sites for hydrogen causing preferentially embrittled paths. Hydrogen produced in the cathodic half cell reaction will also add to the supply of hydrogen used during hydrogen embrittlement. Dissolution (anodic half cell) of active metal, at slip step emergence, at the crack tip will also result in corrosion assisted fatigue crack growth. Sulphide stringers create a large stress concentration ahead of the crack tip thus advancing crack growth. It is true to say that modern steel making practices should be able to reduce the concentration of MnS stringers, thus reducing their rôle in aiding rapid crack advancement.

7.2 General

1. In order to study corrosion fatigue properties of a reactor pressure vessel steel it is important to characterize the steel fully, i.e. mechanical properties, chemical composition, sulphide size, shape and morphology determinations. The corrosion fatigue testing facility would also need to be fully described, i.e. flowrates, water chemistry, mechanical testing unit, specimen potential monitoring, crack length monitoring device etc.

2. Clearly, from the above it is obvious that ASME codes need to be revised to: 1) Give a true 'worst case' crack growth rate curve for reactor pressure vessel steels (air test), or 2) give a list of codes applicable to steels and testing conditions which are well characterized and documented.

3. No 'Paris-Law' type equations have been quoted for the present set of data since only single tests were carried out for each testing variable. Also, it should be obvious that the da/dN versus ΔK curve will vary, depending on the sulphide distribution about the notched C.T. specimen and expected fracture surface. To attempt to produce an equation (Law) governing all similar tests would therefore be ludicrous.

crack tip or diffusion ahead of the crack tip, which would result in embrittled hydrogen diffusion paths. The MnS inclusions act as trap sites for hydrogen causing preferentially embrittled paths. Hydrogen produced in the cathodic half cell reaction will also add to the supply of hydrogen used during hydrogen embrittlement. Dissolution (anodic half cell) of active metal, at slip step emergence, at the crack tip will also result in corrosion assisted fatigue crack growth. Sulphide stringers create a large stress concentration ahead of the crack tip thus advancing crack growth. It is true to say that modern steel making practices should be able to reduce the concentration of MnS stringers, thus reducing their rôle in aiding rapid crack advancement.

7.2 General

1. In order to study corrosion fatigue properties of a reactor pressure vessel steel it is important to characterize the steel fully, i.e. mechanical properties, chemical composition, sulphide size, shape and morphology determinations. The corrosion fatigue testing facility would also need to be fully described, i.e. flowrates, water chemistry, mechanical testing unit, specimen potential monitoring, crack length monitoring device etc.

2. Clearly, from the above it is obvious that ASME codes need to be revised to: 1) Give a true 'worst case' crack growth rate curve for reactor pressure vessel steels (air test), or 2) give a list of codes applicable to steels and testing conditions which are well characterized and documented.

3. No 'Paris-Law' type equations have been quoted for the present set of data since only single tests were carried out for each testing variable. Also, it should be obvious that the da/dN versus ΔK curve will vary, depending on the sulphide distribution about the notched C.T. specimen and expected fracture surface. To attempt to produce an equation (Law) governing all similar tests would therefore be ludicrous.

4. Uncertainty prevails as to when the nozzle region for this project was cut-off the actual nozzle for the nuclear reactor, i.e. at what stage in the heat treatment cycle. However, it is important to realize that neither of the two heat treatments (rough or quality heat treatments) discussed in the text (Section 6.1) would result in changes in the sulphide size, shape or morphology so the results obtained from this work are relevant to the nozzle regions presently found on Kocberg nuclear reactor No. 1.

8.0 REFERENCES

1. P.T. Gilbert: Metallurgical reviews, 1, pp 379-417 (1956).

2. H. Kitegawa: "Corrosion Fatigue, Chemistry, Mechanics and Microstructure", NACE-2, Eds: O. Devereax, A.J. Mc Evily and R.W. Staehle, pp 521-528 (1972).

3. D.J. McAdam, Jnr: "Cong. Inter. Lessai. Materiaux", Amsterdam, pp 305-356 (1928).

4. H.M. Westergaard: J. App. Mech., 6, pp 49-53 (1939).

5. W. Elber: "Damage Tolerance in Aircraft Structures", A.S.T.M., S.T.P. 406, pp 230 (1971).

6. P.C. Paris and F. Erdogen: Transactions of the A.S.M.E. journal of basic engineering, 85, pp 528 (1963).

7. R.N. Parkins: "Some Electrochemical Aspects of the Mechanisms of Corrosion Fatigue", Met. Sci., July 1979, pp 381-386.

8. F.P. Ford: Corrosion, 35, pp 281-287 (1979).

9. P.D. Hicks: FRP Report entitled: "Corrosion Fatigue Testing in Simulated P.W.R. Environments: Literature Survey". Section 2.1.3.1.3.2. University of the Witwatersrand, Metallurgy Department, December 1984.

10. G. Gabetta and R. Rizzi: "Electrochemical Potentials Measured at the tip of a growing fatigue crack in demineralized water 93 °C: The effect of frequency, waveform and oxygen content", presented at the European Federation of Corrosion Meeting on "Low frequency Cyclic Loading Effects in Environment Sensitive Fracture", held in Milan, 9-11 March 1982.

11. I.M. Austin and E.F. Walker: Proc. Int. Conf. on the Effect of Environment on Fatigue, Inst. Mech. Eng. Conf. Publ.

12. P.D. Hicks: FRP Report entitled: "Corrosion Fatigue Testing in Simulated P.W.R. Environments: Literature Survey". Section 2.1.3.1.3.1. University of the Witwatersrand, Metallurgy Department, December 1984.

13. B.F. Brown: "Corrosion Fatigue, Chemistry, Mechanics and Microstructure", NACE 2, pp 25-29 (1972).

14. A.J. Gould: Int. Conf. on Fatigue, Inst. of Mech. Eng., pp 341-347 (1956).

15. W. Marshall: "An Assessment of the Integrity of P.W.R. pressure vessels", U.K.A.E.A., London, March 1982.

16. A Vinckier and A.W. Pense: "A review of underclad cracking in pressure vessel components", W.R.C. 197 (July 1974).

17. W. Marshall: "An Assessment of the Integrity of P.W.R. pressure vessels", U.K.A.E.A., London, H.M.S.O., 1 October 1976.

18. J. Weertman: International Journal of Fracture, 2, pp 460 (1966).

19. B. Tomkins: Philosophical Magazine, 18, pp 1041-1066 (1968).

20. P.E. Irving and L.N. McCartney: Met. Sci., 11, pp 351-361 (1977).

21. P.C. Paris, R.J. Bucci, E.T. Wessel, W.G. Clark and T.R. Mager: ASTM STP 513, pp141 (1972).

22. N.E. Dowling: ASTM STP 601, pp 19-32 (1976).

23. B.O. Johnston: Welding Institute, Report 3592/2/8 (1980).

24. C.E. Richards and T.C. Lindley: Engineering Fracture Mechanics, 4, pp 951 (1972) and C.E.G.B. Report RD/L/N135/78 (1979).

25. M.A. Tolstaya, S.V. Boyatyreva and G.N. Gradusov: Atomnaya Energiya, 10, pp 222-226 (1961), English Translation, pp 231-217 and J. Monahan: Unpublished confirmatory work at A.E.R.E. Harwell.

26. R. Johnson, A. McMinn and B. Tomkins: Proc. I.C.M.-3 Conference, Cambridge, pp 371 (1980).

27. C Amzallag, J.L. Bernard, G. Slama: "Effect of loading and metallurgical parameters on the fatigue crack growth rates of pressure vessel steels in pressurized water reactor environments". International symposium on environmental degradation of materials in nuclear power systems - water reactors, August 22-25 (1983), Myrtle Beach, South Carolina.

28. C. Amzallag, G. Baudry, J.L. Bernard: "Effects of P.W.R. environment on the fatigue crack growth of different stainless steels and Inconel Type Alloy", I.A.E.A.-Specialists' Meeting on Subcritical Crack Growth, Freiburg Federal Republic of Germany, 13-15 May (1981).

29. W.H. Cullen et al.: "Waveform, frequency and temperature effects on the fatigue crack growth rates of pressure vessel steels in high temperature reactor grade water", Report ENSA-81002, 1981 (presented to I.A.E.A. Specialists' Meeting on Subcritical Crack Growth, Freiburg, FRG, pp 13-15, May (1981).

30. W.H. Bamford, D.M. Moon, L.J. Ceshini: "Environmentally assisted crack growth in light water reactor materials", Westinghouse Annual Technical Progress Report (1980).

31. W.H. Bamford, D.M. Moon: "Some mechanistic observations on the crack growth characteristics of pressure vessel and piping steels in P.W.R. environments", Corrosion NACE, Vol. 36, No. 6, June 1980, pp 289-298.

32. W.H. Cullen, K. Törrönen: "A review of fatigue crack growth in pressure vessel and piping steels in high temperature, pressurized reactor-grade water", NUREG (CR-1576, NRL Memorandum Report 4298).

33. W.H. Bamford: "Environmental cracking of pressure vessel boundary materials and the importance of metallurgical considerations", ASME PVP. Conf. Orlando, Fl., pp 209-228 (1982).

34. P.M. Scott and A.E. Truswell: "Corrosion Fatigue crack growth in reactor pressure vessel steels in P.W.R. primary water", ASME PVP Conf. Orlando Fl, pp 271-301 (1982).

35. P.M. Scott, A.E. Truswell: "The influence of water chemistry on fatigue crack propagation in L.W.R. pressure vessel steels", I.A.E.A. Specialists' Meeting on Subcritical crack growth, 13-15 May (1981), Freiburg, FRG, NUREG/CP - 0044 - Vol. 2, pp 91-126.

36. J.D. Atkinson and T.C. Lindley: "The influence of environment on fatigue", Inst. Mech. Eng Publications, 4, pp 65-74 (1977).

37. T.R. Mager, D.M. Moon, J.D. Landes: Trans. of the ASME J. of Pressure Vessel Technology, 99, pp 238-247 (1977).

38. H. Hänninen, K. Törrönen, M. Kempainen and S. Solonen: "On the mechanisms of environment sensitive cyclic crack growth of nuclear reactor pressure vessel steels", Presented at the European Federation of Corrosion Meeting on "Low frequency cyclic loading effects in environment sensitive fracture" held in Milan, 9-11 March 1982.

39. M. Suzuki, H. Takahashi, T. Shoji, T. Kondo, H. Nakajima: "The environment enhanced crack growth effects in structural steels for water cooled nuclear reactors", I. Mech. Eng., pp 161-169 (1977).

40. L.A. James: "Fatigue crack propagation in neutron-irradiated ferritic pressure-vessel steels", Nuclear Safety, Vol. 18, No. 6, Nov-Dec 1977.

41. W.H. Cullen: "Effects of Irradiation and Temperature on Fatigue Crack Growth Rates of A508-2 Steel in P.W.R. Environment", Paper presented to the I.C.G.G.R., June, 1984.

42. T. Kondo, T. Kikayama, H. Nakajima, M. Shindo and R. Nagasaki: "Corrosion Fatigue of A.S.T.M. A-302B steel in high temperature water, the simulated nuclear reactor environment", Proc. 1st International Conf. on Corrosion Fatigue, NACE, pp 539 (1972).

43. M.E. Indig, J.E. Weber, D. Weinstein: "Environmental aspects of carbon steel stress corrosion in high purity water", Reviews on coatings and corrosion, Vol. 5, pp 174-224 (1982).

44. M.E. Indig and A.R. McIlree: Corrosion, 35, pp 228, July 1979.

45. J. Vagner, F. Robinson, G. Slama, L. Bernard, C. Duchalet and A. Pelisier-Tanon: I.A.E.A. Specialists' Meeting on Reliability Engineering and Lifetime assessment of Primary system Components, Vienna, 1-3 Dec 1980 and Framatome Seminar on "Underclad cracking analysis and solution, 20-23 May 1981.

46. W.H. Bamford: Trans. of the ASME, J. of Engineering Materials and Technology, 101, pp 73-79 (1979).

47. P. Rabbe, C. Amzallag and J.P. Raoul: Creusot-Loire Report 1128 (August 1974).

48. W.H. Bamford, D.M. Moon, L.J. Ceshini: "Crack growth rate testing in reactor pressure vessel steels", proceedings of the fifth water reactor safety information meeting, Gaithesburg, Md, Nov 1977.

49. R. Achilles: M.Sc. dissertation at The University of the Witwatersrand; 1985

50. P.D. Hicks: B.Sc. Thesis at the University of the Witwatersrand, Sept. 1983, SA. "The influence of ion implantation on the corrosion performance of 3CR12".

51. C.E. Sims and F.B. Dahle: Trans. A.F.A., 1938, 46, pp.65-132.

52. M. Pourbaix: "Thermodynamics des Solutions aqueuses diluées" (Meinema, Delft), or J.N. Agars translation: "Thermodynamics of Dilute Aqueous Solutions" (Arnold).

53. Private communications with Dr P. Scott (Harwell).

54. Private communications with Dr J. Bulloch (University of the Witwatersrand).

55. Document issued to ESCOM (Confidential category F). "Generic Material Data, Low Alloy Mn-Ni-Mo Pressure Vessel Steels".

56. P.D. Hicks: "Report on May/June 1984 visit to the United Kingdom" July 1984, FRP/C/84/27, Appendix III. University of the Witwatersrand, South Africa.

57. D.A. Skoog and D.M. West: "Fundamentals of Analytical Chemistry". Third Ed., pp. 379.

58. M.O. Speidel et al.: "Proc. Int. Conf. on Corrosion Fatigue, Storrs, Connecticut, 1971 (NACE), pp. 324.